Tectonophysics 767 (2019) 128158

Contents lists available at ScienceDirect

Tectonophysics

journal homepage: www.elsevier.com/locate/tecto

Deciphering the tectono-metamorphic evolution of the Nevado-Filábride complex (Betic Cordillera, Spain) – A petrochronological study

Ángel Santamaría-López[a,*], Pierre Lanari[b], Carlos Sanz de Galdeano[c]

[a] Departamento de Química Inorgánica, Cristalografía y Mineralogía, Facultad de Ciencias, Universidad de Málaga, 29071 Málaga, Spain
[b] Institute of Geological Sciences, University of Bern, Baltzerstrasse 1+3, 3012 Bern, Switzerland
[c] Instituto Andaluz de Ciencias de la Tierra, Consejo Superior de Investigaciones Científicas–Universidad de Granada, Facultad de Ciencias, 18071 Granada, Spain

ARTICLE INFO

Keywords:
Nevado-Filábride complex
Garnet thermobarometry
Allanite dating
XMapTools
GrtMod

ABSTRACT

The Nevado-Filábride metamorphic complex (Betic Cordillera, Spain) exhibits a succession of Paleozoic and Mesozoic metasediments, orthogneisses and metabasites. The complex has been divided into three tectono-metamorphic units, from bottom to top: the Ragua, Calar-Alto and Bédar-Macael units. The petrochronological evolution of the complex is not well constrained as P-T-t conditions differ between authors mainly because of the investigated rock types and the thermobarometric and geochronological techniques applied. Five garnet-bearing mica-schists from various areas of the complex were investigated for constraining and comparing the shape of the P-T paths recorded by the three units. Quantitative compositional mapping of garnet and K-white mica was combined with iterative thermodynamic models. The resulting P-T trajectories suggest that the units experienced similar clockwise P-T trajectories during Alpine metamorphism. The three units reached high-pressure and low-temperature conditions of ~2.0 GPa and ~520 °C in the Bédar-Macael unit; ~2.0–2.2 GPa and ~470–490 °C in the Calar-Alto unit; and ~2.2 GPa and ~480 °C in the Ragua unit. All samples recorded a temperature increase of ~130 °C during exhumation as shown by the successive stages of white mica re-equilibrations. Heating during exhumation was probably triggered by the hot hanging wall over the Nevado-Filábride complex. The garnet rims reflect a high-temperature and low-pressure stage which was dated at ~13 Ma using allanite U-Th-Pb geochronology (LA-ICP-MS). Following the temperature peak, exhumation continued associated to cooling. Similarities in the shapes of P-T path throughout the units suggest a continuous metamorphic sequence rather a tectonically divided complex.

1. Introduction

Pressure-Temperature-time (P-T-t) path summarizes the changes in pressure and temperature conditions that have been recorded in a rock sample during an orogeny. In order to decipher mountain-building tectonic processes such as the subduction and exhumation of metamorphic complexes, P-T-t paths for metamorphic rocks of several units are required (e.g. Ernst, 1988; Guillot et al., 2009; Rolland et al., 2012). Quantification of the differences or similarities in the conditions recorded by several tectonic units is a great help in deciphering possible tectonic scenarios and in resolving tectonic and thermal histories (e.g. Thompson and England, 1984; Jamienson, 1991; Foster and Parrish, 2003; Brown, 2014).

The development of analytical and modelling techniques in metamorphic petrology has opened new possibilities for thermobarometry and improved our ability to reconstruct portions of P-T paths (e.g. Brown, 2007, 2014; Lanari et al., 2019; Lanari and Duesterhoeft, 2019). Thermobarometric methods include empirical thermobarometers (e.g. Hodges and Crowley, 1985), multi-equilibrium or *average P-T* approach (e.g. Holland and Powell, 1998; Berman, 1991) equilibrium phase diagrams (e.g. Holland and Powell, 1998, 2011), Raman spectrometry on carbonaceous material (e.g. Beyssac et al., 2002), etc. Generally, these techniques are based on the assumption of chemical equilibrium and have absolute uncertainties of ± 50 °C (Kohn and Spear, 1991). By contrast, relative errors are smaller, allowing relative thermobarometry between units to be performed in a much precise way (Worley and Powell, 2000).

Thermobarometry requires the knowledge of the composition of minerals assumed to have been in chemical equilibrium at a given stage of their metamorphic history. Resilient porphyroblasts are excellent candidates as they can preserve chemical and textural record of metamorphic conditions affected the rock (e.g. Lanari et al., 2017;

* Corresponding author.
E-mail addresses: angelsan83@correo.ugr.es (Á. Santamaría-López), pierre.lanari@geo.unibe.ch (P. Lanari), csanz@ugr.es (C. Sanz de Galdeano).

https://doi.org/10.1016/j.tecto.2019.06.028
Received 24 July 2018; Received in revised form 24 June 2019; Accepted 29 June 2019
Available online 05 July 2019
0040-1951/

Yakymchuk et al., 2017). This is the case of garnet which is a common rock-forming mineral often preserving compositional zoning interpreted to reflect changes in equilibrium conditions (Gaidies et al., 2008; Caddick and Kohn, 2013; Cheng and Cao, 2015; Baxter et al., 2017; Lanari and Engi, 2017). For that purpose, the application of quantitative compositional mapping has proven to be of great help to image compositional zoning and relate these to P-T conditions of growth (Lanari et al., 2013, 2014, 2019). However, as garnet grows, it becomes isolated from the reactive part of the rock and the thermobarometric reconstruction based on bulk rock compositions are biased (Spear, 1988; Evans, 2004; Tinkham and Ghent, 2005). An alternative strategy to confront this problem is that followed by Lanari et al. (2017) which allows P-T conditions to be refined using an iterative optimization process based on the composition of each successive growth zones. Resorption and fractionation of garnet previously formed are optimized to assess the possible variations of the reactive bulk composition.

The collision of the African and Iberian plates led to the formation and staking of three metamorphic complexes included in the Internal Zone of the Betic Cordillera and named from bottom to top: the Nevado-Filábride, the Alpujárride and the Maláguide. In numerous studies, it has been proved that the Nevado-Filábride complex was affected by metamorphism during the Alpine orogeny (e.g. Augier et al., 2005b; Platt et al., 2005; Platt et al., 2006). Although several studies suggested that the Nevado-Filábride metamorphic history is characterized by an early Alpine HP/LT metamorphism followed by decompression at LP/HT, no consensus has been reached regarding the shape of the P-T-t trajectories recorded by each unit of this complex (Gómez-Pugnaire and Fernández-Soler, 1987; Bakker et al., 1989; Vissers et al., 1995; López-Sánchez-Vizcaíno et al., 2001; Puga et al., 2002; Augier et al., 2005a, 2005b; Behr and Platt, 2012; Ruiz-Cruz et al., 2015; Li and Massonne, 2018). The published P-T paths are scattered in particular for the decompression history. Differences strongly depend on the rock types and the thermobarometric methods applied, thus preventing the comparison to be made with a high degree of confidence. Another subject of debate is the division of the Nevado-Filábride complex into large-scale units (e.g.; Puga et al., 1974; Puga et al., 2002; Martínez-Martínez et al., 2002; Aerden and Sayab, 2008), which besides of lithological and structural criteria, is mainly based on differences in the metamorphism record observed in the upper and lower part of the complex. A complete discussion about the proposed division should take into account similarities and differences between the proposed units in regards to lithology, affinity, geochronological data, and the characterization of shear zones between units (e.g. ductile to ductile-brittle shear zones previously proposed for the contact between units; e.g. Martínez-Martínez et al., 2002). It also strongly relies on a better knowledge and comparison of the P-T paths from the lower and upper parts. The petrochronological constraints are also quite limited; according to previous studies, HP/LT metamorphism happened either before 30 Ma (Monié et al., 1991; Augier et al., 2005a; Li and Massonne, 2018) or during Miocene (López-Sánchez-Vizcaíno et al., 2001; Platt et al., 2006; Gómez-Pugnaire et al., 2012). Dating of the LP/HT metamorphism and the coeval exhumation is still partially unconstrained (Augier et al., 2005a; Li and Massonne, 2018).

In this work, we investigated five garnet-bearing mica-schists taken from different areas and sections of the Nevado-Filábride complex. High-resolution electron probe micro-analyser (EPMA) compositional mapping of garnet and white mica was combined with iterative thermodynamic models (Lanari et al., 2017) to obtain the P-T conditions of garnet and white mica growth in different units using the same modelling technique and set of thermodynamic data. The subduction and exhumation histories of the complex were refined based on the comparison of the shape of the P-T paths of the upper and lower units. The P-T paths obtained for the Nevado-Filábride complex were combined with in situ U-Th-Pb allanite dating in an attempt to add time-constraints on the P-T evolution. Allanite was selected in this study as it has been demonstrated to be a robust mineral chronometer (Engi, 2017). Allanite is known to retain its chemical and isotopic characteristics to temperature higher than 600 °C even in shear zones where it experienced intense deformation and strong fluid rock interactions (Cenki-Tok et al., 2011).

2. Geological settings

2.1. The Betic Cordillera

The Betic Cordillera is located in the S and SE of the Iberian Peninsula (Fig. 1) and constitutes, with the Rif, the westernmost part of the Mediterranean Alpine Belt. The Betic-Rif Cordillera resulted from the convergence of the African and Iberian plates (e.g. Didon et al., 1973; Durand-Delga and Fontboté, 1980; Vera, 2004; Aerden et al., 2013), which lead to the collision of several pre-Miocene tectonic domains (e.g. Durand-Delga and Fontboté, 1980; Bouillin et al., 1986; Augier et al., 2005b). The Betic Cordillera is made of an External and Internal zone. The External Zone is formed by Mesozoic and Tertiary sedimentary successions which constitute the sedimentary cover of the S and SE prolongations of the Paleozoic Iberian Massif. The Internal Zone (also known as “Alborán domain”, see Balanyá and García-Dueñas, 1987) is formed by a Paleozoic basement and a Mesozoic cover. The Internal Zone has been traditionally divided into three (e.g. Egeler and Simon, 1969; Martínez-Martínez et al., 2002; Vera, 2004) or four (Puga et al., 2002) complexes. The uppermost one, the Maláguide complex, includes Paleozoic sediments and a Mesozoic and Tertiary discontinuous cover, both not metamorphosed or barely metamorphosed (Mäkel, 1985; Vera, 2004; Sanz de Galdeano et al., 2006). The intermediate one, the Alpujárride complex is mainly formed by Paleozoic and Mesozoic metasediments, which recorded an early HP/LT Alpine metamorphism with a minimum age of 21–23 Ma (Goffé et al., 1989; Azañón and Goffé, 1997; Sánchez-Rodríguez and Gebauer, 2000; Booth-Rea et al., 2002; Janots et al., 2006) followed by a low pressure and locally high temperature stage (Platt et al., 2013). The lower complex, which is investigated in this study, is known as the Nevado-Filábride complex, and is formed by mica-schists (mainly), quartzites, marbles, orthogneisses and metabasites. The contact between both complexes is characterized by a ductile to brittle low-angle normal fault formed during the exhumation process (Galindo-Zaldívar et al., 1989; Jabaloy et al., 1993; Augier et al., 2005c; Agard et al., 2011; Jabaloy et al., 2015).

According to Santamaría-López and Sanz de Galdeano (2018) the maximum age of deposition of the mica-schists protolith is ca. 349 Ma.

2.2. Nevado-Filábride complex division

Several tectonic and tectono-metamorphic models have been proposed in the literature, but each of them strongly relies on how the units within the Nevado-Filábride complex are defined. Brouwer (1926) first distinguished two formations based on lithological criteria: the lowermost Crystalline of Sierra Nevada and the Mischungszone – mixed – zone. Since that, the division has remained a matter of debate depending on the criteria used by each author (i.e. petrological, structural and/or metamorphic). According to Puga et al. (1974) and Puga and Díaz de Federico (1976), the Nevado-Filábride complex is divided into the Veleta nappe (equivalent to the Crystalline of Sierra Nevada), and the overlaying Mulhacén nappe (approximately equivalent to the Mischungszone). The Veleta nappe contains a monotonous sequence of dark schists (graphite-bearing) and quartzites, whereas the Mulhacén nappe shows a larger variety of lithologies such as light and dark schists, quartzites, marbles, gneisses, serpentinites and amphibolites. Puga et al. (2002) reclassified as “complexes” the “nappes” of Puga and Díaz de Federico (1976). Martínez-Martínez et al. (2002) renamed the Veleta nappe as Ragua unit (being not exactly, but approximately equivalents), and subdivided the Mulhacén nappe into the lowermost Calar-Alto unit and the overlying Bédar-Macael unit. However, authors

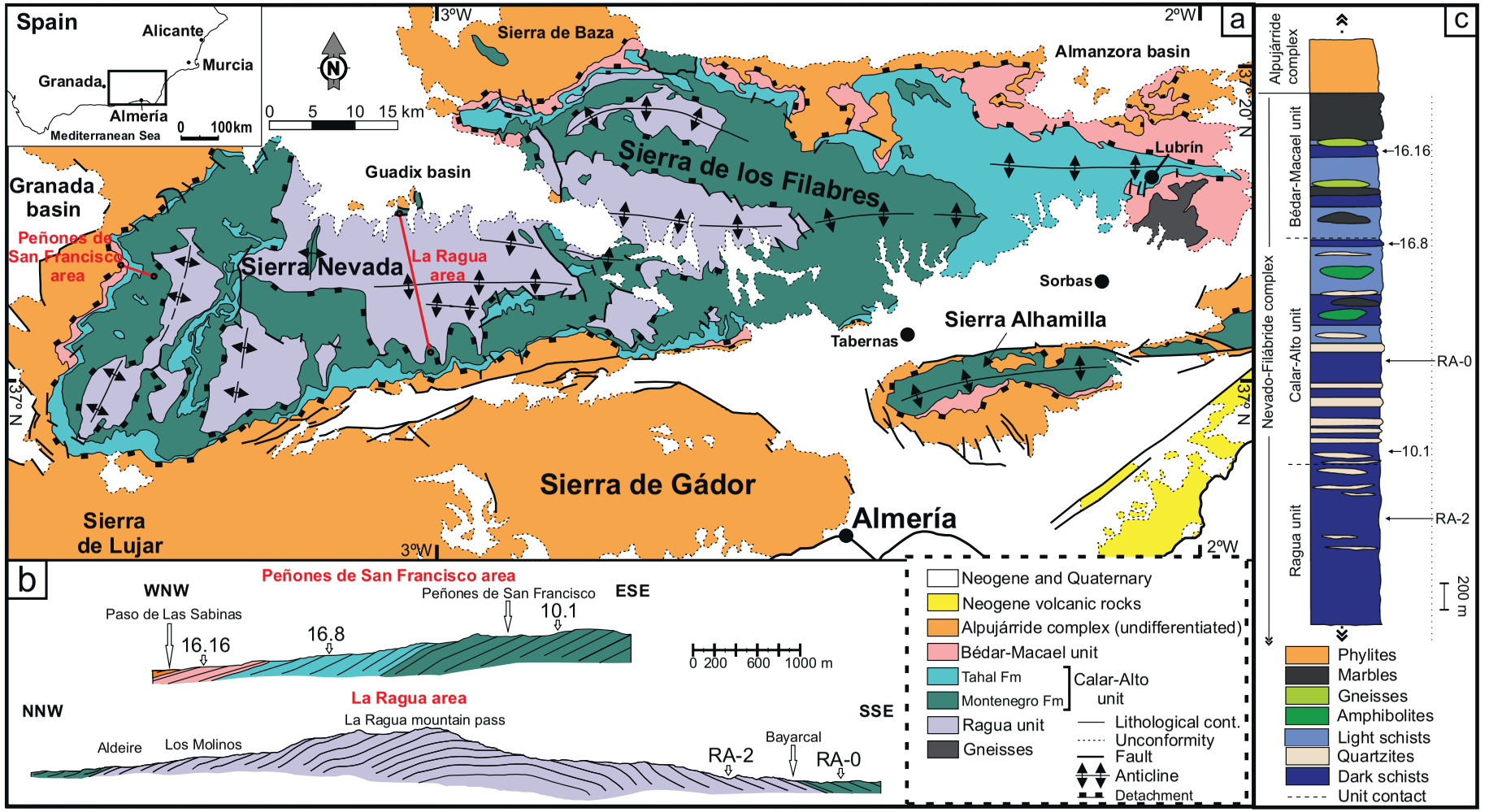

Fig. 1. Geological map and transects of the southeast Iberian Peninsula. **a** General map of the Betic cordillera showing the Nevado-Filábride complex distribution. Sampling areas: Peñones de San Francisco and La Ragua, are shown as lines labeled as 1 and 2 respectively. **b** Geological cross sections of the Peñones de San Francisco and La Ragua areas. **c** Schematic lithological succession of the Nevado-Filábride Complex including the sample location.

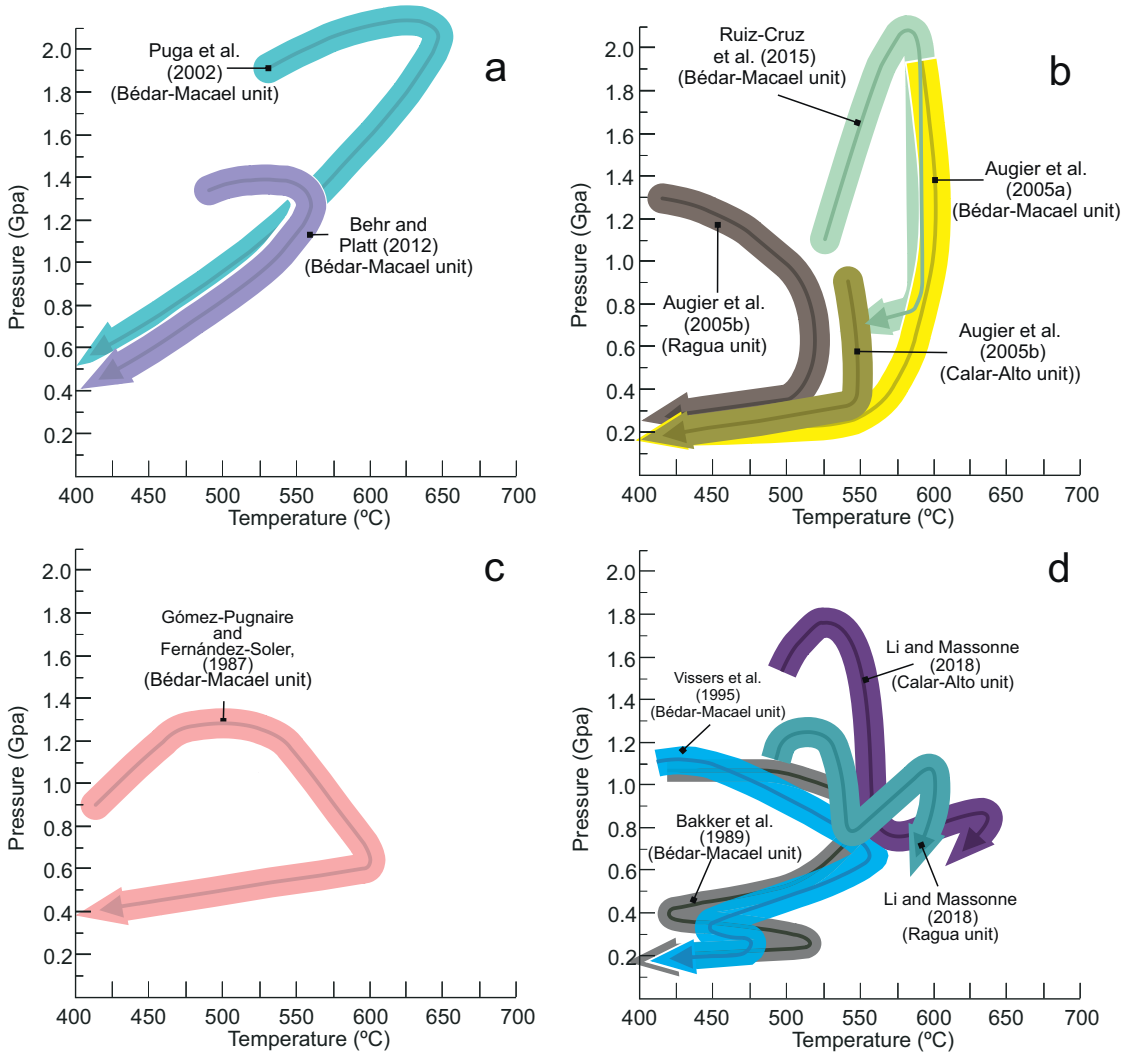

Fig. 2. P-T trajectories previously published for the Nevado-Filábride Complex: **a** hairpin trajectories, **b** isothermal decompression, **c** slight heating upon decompression, **d** late reheating.

as Galindo-Zaldívar (1993), Sanz de Galdeano and López-Garrido (2016) and Sanz de Galdeano et al. (2016) have rather suggested a continuous lithological sequence in the Nevado-Filábride complex.

The location and even existence of the tectonic units remains imprecise nowadays despite the number of studies focused on the complex. In the present study the division used by Martínez-Martínez et al. (2002) has been adopted because its use in several recent studies of metamorphic conditions in the Nevado-Filábride complex (e.g. Platt et al., 2013; Kirchner et al., 2016; Li and Massonne, 2018). According to several authors (e.g. Martínez-Martínez et al., 2002; Augier et al., 2005a; Booth-Rea et al., 2015) the contact between the Ragua and Calar-Alto, and the Calar-Alto and Bédar-Macael units correspond to ductile shear zones.

2.3. Metamorphism in the Nevado-Filábride complex

Several lines of evidence suggest a two-stage metamorphic history with a HP/LT Alpine stage followed by a LP/HT stage during decompression. This latest stage largely overprinted the previous metamorphic record particularly, but not exclusively, in the metasediments. A few metamorphic studies were focused on metapelites (Augier et al., 2005a, 2005b; Ruiz-Cruz et al., 2015) and most of the constraints for the HP/LT stage are from the studies focused on mafic and felsic igneous rocks (e.g. Gómez-Pugnaire et al., 1994; López-Sánchez-Vizcaíno et al., 2001, 2005; Puga et al., 2000, 2002; Padrón-Navarta et al., 2010; Ruiz-Cruz et al., 2015). However, the P-T estimates obtained in each lithology point toward a two-stage metamorphic history with HP/LT conditions and LP/HT conditions (Fig. 2). The resulting P-T paths however, strongly differ between authors, in particular for the decompression stage. Puga et al. (2000, 2002) and Behr and Platt (2012) proposed hairpin trajectories (Fig. 2a), which show coincidence in the P and T peaks; Augier et al. (2005a, 2005b), Ruiz-Cruz et al. (2015) and Laborda-López et al. (2018) suggested an isothermal decompression (Fig. 2b); Gómez-Pugnaire and Fernández-Soler (1987) proposed slight heating upon decompression (Fig. 2c); and Vissers (1981), Bakker et al. (1989), Booth-Rea et al. (2015) and Li and Massonne (2018) pointed to the existence of late reheating at lower pressure conditions (Fig. 2d). Discrepancies between authors have been attributed either to differences between thermobarometers, or variations of P-T trajectories throughout the cordillera (Platt et al., 2013).

2.4. Age constraints

Similarly to the internal division of the Nevado-Filábride complex and its P-T history, there is no consensus regarding the age of each metamorphic stage. Augier et al. (2005a) applied in situ laser $^{40}Ar/^{39}Ar$ on K-white mica in metapelite samples from Calar-Alto and Bédar-Macael units. They concluded that the HP/LT stage took place at ca.

Table 1
Bulk compositions from studied samples used for modelling.

Sample	16.16	16.8	RA-0	10.1	RA-2
SiO_2	60.19	57.24	53.00	59.33	75.10
TiO_2	0.42	0.50	1.46	0.61	0.80
Al_2O_3	20.35	19.91	23.29	19.18	12.04
FeO	10.86	7.60	8.93	9.44	4.49
MnO	0.12	0.30	0.12	0.41	0.04
MgO	2.51	2.10	1.24	2.30	1.00
CaO	0.82	2.29	0.30	1.27	0.25
Na_2O	1.29	1.99	0.89	1.29	0.65
K_2O	2.55	2.14	3.29	2.24	1.81

30 Ma (or possibly later), and was followed by the main exhumation between 22 and 18 Ma and the last step of exhumation between 14 and 9 Ma. According to Li and Massonne (2018) the HP/LT event occurred during Eocene (~40 Ma), and it was followed by a second P-T loop during exhumation at 24.1 ± 0.8 Ma. Other studies reported younger Miocene ages for the pressure peak conditions including López-Sánchez-Vizcaíno et al. (2001) (15.0 ± 0.6 Ma) and Gómez-Pugnaire et al. (2012) (17.3 ± 0.4 Ma) based on U—Pb dating of zircon from the upper part of the Nevado-Filábride complex; Platt et al. (2006) who obtained ages ranging between 18 and 14 Ma from Lu—Hf dating of garnet separates in mafic eclogites and schists from several parts of the Nevado-Filábride complex; and Kirchner et al. (2016) who applied multimineral $^{87}Rb/^{86}Sr$ geochronology to date the HP/LT event ~20–13 Ma. Monié et al. (1991) obtained an integrated $^{40}Ar/^{39}Ar$ age range of 48.4 ± 3.3 Ma on amphibole from the metabasites for the HP/LT event in the upper part of the complex. Behr and Platt (2012) obtained zircon fission track ages of ~16–13 Ma; and Platt et al. (2006) and Behr and Platt (2012) apatite fission track ages ranging between ~19 and 6 Ma. Johnson et al. (1997) yielded apatite and zircon fission track ages 12–8 Ma. In addition, de Jong (2003) obtained whole-rock-phengite Rb—Sr dates of ~14 and ~17 Ma, representing isotopic re-equilibration during the early stages of exhumation.

As a summary, and according to previous studies, the HP/LT event should have occurred not after the Miocene (48 to 13 Ma). On the other hand, the LP/HT stage has not been extensively dated, with the exception of Augier et al. (2005a) and Li and Massonne (2018).

3. Methods

The petrochronology strategy used in this study involved the following steps (see Engi et al., 2017 for a detailed description): (1) classical thin section analysis for petrography, (2) quantitative compositional mapping combined with iterative thermodynamic modelling to retrieve P-T conditions and (3) in situ U-Th-Pb allanite dating. The analytical and computational methods employed are described in the following sections.

3.1. Petrography

Five mica-schist samples from two areas of the Nevado-Filábride complex were investigated in this study (samples 16.16, 16.8, 10.1, RA-0 and RA-2, see Section 4). The studied samples were investigated first by optical microscopy and scanning electron microscopy (SEM) using an Environmental Scanning Electron Microscope (ESEM) FEI model Quanta 400, operating at 15–20 keV in Centro de Instrumentación Científica (CIC), Universidad de Granada (Spain). Allanite grains were identified in backscattered electron (BSE) images using a ZEISS EVO 50 scanning electron microscope at the Institute of Geological Sciences, University of Bern.

3.2. Bulk-rock composition

X-ray fluorescence (XRF) analyses of major elements of whole rocks were carried out with a Philips PW1040/10 spectrometer in the Centro de Instrumentación (CIC, Universidad de Granada, Spain). The detection limit for major elements was 0.01 wt%. Loss on ignition (LOI) was determined with 0.5 g of powdered sample, first dried at 110 °C and then heated to 1000 °C for 1 h.

Representative bulk rock compositions were determined for samples 16.16, 16.8, 10.1 following the technique described in Laurent et al. (2018). In order to check the reliability of these estimates the same technique was applied for samples RA-0 and RA-2, and the modelling results were compared with those of obtained by XRF. The estimated bulk rock composition in samples RA-0 and RA-2 and the P-T conditions for garnet are similar within uncertainty. The bulk rock compositions used for modelling are reported in Table 1.

3.3. Quantitative compositional mapping

Two sets of compositional maps for major elements were obtained by EPMA. The first set of map was focused on garnet porphyroblasts and the second on micas in the mineral matrix. The analyses were carried out at the Institute of Geological Sciences, University of Bern, using a JEOL JXA-8200 superprobe instrument. The detailed analytical procedure is given in Lanari et al. (2013, 2014). The analytical conditions were 15 keV accelerating voltage, 100 nA specimen current, and variable dwell times. Dwell times for garnet maps were 100 ms (samples 10.1 and 16.16); 150 ms (sample RA-0); and 200 ms (samples 16.8 and RA-2). Dwell times for white-mica maps were 200 ms (samples RA-2, 10.1 and RA-0) and 160 ms (samples 16.16 and 16.8). The dwell time used in each analytical session was based on the analytical time available and the size of the mapped areas. The sizes of the garnet maps are: 948 × 1228 μm for sample 16.16; 2200 × 2200 μm for sample 16.8; 1800 × 1800 μm for sample RA-0; 770 × 900 μm for sample 10.1; and 800 × 800 μm for sample RA-2. The sizes of mica maps are: 400 × 600 μm for sample RA-2; 2010 × 900 μm for sample 10.1; 800 × 1200 μm for sample RA-0; 1050 × 2100 μm for sample 16.16; 1050 × 2100 μm for sample 16.8. For both datasets, nine elemental maps were acquired in two passes (Si, Mg, Na, Ca, K and Ti, Al, Fe, Mn). Data processing and calibration were performed using XMapTools 2.6.4 (Lanari et al., 2014, 2019). The analytical standardization was performed using the composition of high-quality spot analyses acquired on the same area (de Andrade et al., 2006) and the advanced procedure described in Lanari et al. (2019).

3.4. Phase equilibria modelling

Following the strategy described in Lanari et al. (2017), P-T conditions of garnet growth were obtained for each successive growth zone of 5 selected porphyroblasts. These grains were carefully selected based on BSE images and point analyses. The selection criteria applied in this study included the size of the porphyroblast, the preservation and absence of retrogression and their low inclusion content. Pixels showing mixing compositions, either along the grain boundaries or around mineral inclusions were filtered out using the *BRC* function of XMapTools (Lanari et al., 2019). A representative composition of each growth zone was obtained by averaging pixels from manually selected spatial domains. The corresponding compositions and their analytical uncertainties were exported and are reported in Table 2.

The composition of each successive growth zones were used to model the P-T-X conditions of garnet growth by using the program GrtMod 1.5.3 (Lanari et al., 2017). This program provides a numerical simulation of the garnet evolution based on the composition of the successive growth zones characterized in the compositional maps, combined with an iterative modelling strategy. This model relies on predictions made by Gibbs free energy minimization and the program

Table 2
Representative mineral compositions of garnet.

Sample	16.16			16.8			RA-0				10.1				RA-2	
Grt	Grt_1	Grt_2	Grt_3	Grt_1	Grt_2	Grt_3	Grt_1	Grt_2	Grt_3	Grt_4	Grt_1	Grt_2	Grt_3	Grt_4	Grt_1	Grt_2
SiO_2	38.727	38.419	38.575	37.328	37.595	37.702	37.853	37.668	38.209	38.032	37.422	36.588	37.616	37.741	38.072	37.880
Al_2O_3	21.425	21.356	21.478	20.629	20.738	20.784	21.905	21.867	22.159	21.995	20.657	20.359	20.713	20.788	21.307	21.455
FeO	31.007	36.171	35.600	26.648	28.525	29.748	28.479	30.139	28.726	30.567	27.669	29.460	30.927	31.013	26.499	30.140
MnO	1.879	0.447	0.207	3.990	1.631	0.461	3.480	2.280	0.760	0.557	5.133	3.810	1.327	0.680	5.488	1.625
MgO	1.903	3.954	3.836	0.951	1.395	1.994	0.682	0.776	0.918	1.169	1.138	1.163	1.301	1.344	0.605	0.806
CaO	6.976	2.168	2.786	9.057	9.461	8.838	8.907	8.249	10.793	8.776	7.498	6.554	8.306	8.965	9.515	9.344
Na_2O	0.023	0.015	0.014	0.120	0.090	0.132	0.066	0.045	0.039	0.041	0.041	0.047	0.027	0.026	0.060	0.043
K_2O	0.003	0.002	0.003	0.015	0.008	0.007	0.023	0.023	0.024	0.023	0.010	0.020	0.009	0.009	0.013	0.008
Atom site distribution (12 anhydrous-oxygen basis)																
Si(O/T)	3.031	3.002	3.007	3.021	3.014	3.012	2.988	2.986	2.988	2.995	3.019	3.008	3.013	3.008	3.006	2.996
Al(Y)	1.976	1.967	1.974	1.967	1.960	1.957	2.038	2.043	2.043	2.042	1.964	1.973	1.955	1.953	1.982	2.000
Fe(X)	2.030	2.364	2.321	1.804	1.913	1.988	1.880	1.998	1.879	2.014	1.867	2.026	2.072	2.068	1.750	1.994
Mg(X)	0.222	0.461	0.446	0.115	0.167	0.238	0.080	0.092	0.107	0.137	0.137	0.143	0.155	0.160	0.071	0.095
Mn(X)	0.125	0.030	0.014	0.273	0.111	0.031	0.233	0.153	0.050	0.037	0.351	0.265	0.090	0.046	0.367	0.109
Ca(X)	0.585	0.181	0.233	0.785	0.813	0.757	0.753	0.701	0.904	0.741	0.648	0.577	0.713	0.766	0.805	0.792
X_{alm}	0.685	0.779	0.770	0.606	0.637	0.660	0.638	0.679	0.639	0.688	0.622	0.673	0.684	0.680	0.585	0.667
X_{prp}	0.075	0.152	0.148	0.039	0.056	0.079	0.027	0.031	0.036	0.047	0.046	0.047	0.051	0.053	0.024	0.032
X_{sps}	0.042	0.010	0.005	0.092	0.037	0.010	0.079	0.052	0.017	0.013	0.117	0.088	0.030	0.015	0.123	0.036
X_{grs}	0.198	0.060	0.077	0.264	0.271	0.251	0.256	0.238	0.308	0.253	0.216	0.192	0.235	0.252	0.269	0.265

THERIAK-DOMINO (version 04.02.2017, and database of Holland and Powell (1998) and subsequent updates provided in Supplementary Material S1), including an optimization of the reactive bulk composition. Three variables are optimized, P, T, and for stages *n + 1*, the volume fraction of all the previous growth zones fractionated from the bulk-rock composition. So, the reactive bulk composition of stage *n + 1* is estimated by fractionating a variable amount of the garnet previously formed (see details in Lanari et al., 2017). Previously formed garnet can thus be isolated from the reactive part of the rock (fractionation) or dissolve (resorption), i.e. partly react to form the new garnet generation. The predicted garnet composition for any P-T-X conditions is compared to the reference composition obtained from the map. By minimizing the differences between the measured and the modelled compositions obtained from each effective bulk composition (using the Nelder–Mead algorithm, a heuristic search method; Nelder and Mead, 1965) the program leads to constrain the optimal P-T-X condition for each growth stage.

The compositions of K-white mica extracted from the compositional maps were compared with the modelled compositions based on two compositional variables: Si (atoms per formula unit, apfu) and XMg ($Mg/(Mg^{+}+Fe^{2+})$, with Mg and Fe in apfu, assuming no ferric iron, $Fe^{3+}=0$). For each Si-XMg pairs (5000 pixel compositions of K-white mica were randomly selected from each map), the optimal conditions were determined using the intersection between these two isopleths. This procedure is similar to that followed for garnet, as in both cases, the optimal P-T condition is derived by comparing the measured and modelled compositions. In the case of K-white micas, only two independent variables are involved (leading to a "perfect" P-T solution marked by the intersection of two isolines or an absence of solution with the intersection do not occur in the P-T range) and fractionation effects for white mica are negligible (Airaghi et al., 2017). This is not possible for garnet (3–4 isolines) for which a weighted procedure is required to obtain "optimal" P-T conditions (Lanari and Duesterhoeft, 2019). In addition fractionation effects are strong and can significantly affect the P-T results (Lanari and Engi, 2017 and references therein). P-T estimates from K-white mica are presented as ellipses in the P-T diagrams computed assuming a generic uncertainty of ± 0.01 for both Si (apfu) and XMg (1σ). The relative and absolute uncertainties were estimated using a Monte Carlo simulation and a single K-white mica composition. The relative uncertainty, based on counting statistics, is 3.151 ± 0.006 apfu for Si^{4+} and 0.541 ± 0.008 for XMg. The total uncertainty including the relative uncertainty and the absolute uncertainty, estimated using the external reproducibility, is 3.151 ± 0.011 apfu for Si^{4+} and 0.541 ± 0.015 for XMg. Therefore the generic uncertainty proposed above (± 0.01) is relevant to visualize how the relative uncertainty in composition affects the P-T conditions.

3.5. Th-U-Pb allanite dating by LA-ICP-MS

Allanite dating was carried out at the Institute of Geological Sciences, University of Bern by using a LA-ICP-MS GeoLas Pro 193 nm ArF excimer laser coupled to an Elan Dynamic Reaction Cell (DRC-e) ICP-MS. The analytical procedure is described in Burn et al. (2017). Pre-ablation was performed for four to five pulses with an energy density of 2.5 J cm^{-2}, a repetition rate of 1 Hz, and spot sizes of 40 and 32 µm. Ablation was performed with an energy density of 2.5 J cm^{-2}, a repetition rate of 9 Hz, and spot sizes of 32 and 24 µm. A gas mixture of He (1 L min^{-1}) and H_2 (0.08 L min^{-1}) was used for aerosol transport from the ablation cell to the plasma. Settings on instrument were optimized to increase the sensitivity of heavy masses (e.g. ^{238}U, ^{232}Th, ^{206}Pb, ^{207}Pb, ^{208}Pb). Oxide production (ThO+/Th+) was kept lower than 0.5%. NIST SRM 610 measurements were performed for quantify U and Th concentrations. Plešovice zircon (Sláma et al., 2008) was used as primary standard. In order to minimize instrumental drift the acquisition series were approximately 1 h, including between 8 and 12 unknown analyses bracketed by 8 analyses of the standard Plešovice used for U–Th–Pb ratio calibration and SRM 610 for trace element calibration. Analyses were guided by SEM (BSE) images in order to identify internal texture and compositional zoning in allanite. Data reduction was carried out using the in-house software TRINITY (Burn et al., 2017).

4. Quantitative petrography

Among the five investigated samples, three of them, 10.1, 16.8 and 16.16, were collected in the Peñones de San Francisco area in the westernmost part of the Sierra Nevada range. The two other samples, RA-2 and RA-0, come from La Ragua area in the central part of the range (Fig. 1a). The position of the samples is shown in Fig. 1c.

4.1. Mineral assemblages

Samples are described from lower to higher position in the Nevado-Filábride complex (Fig. 1c).

Sample RA-2 is a fine grained dark mica-schist (Fig. 3a) selected in

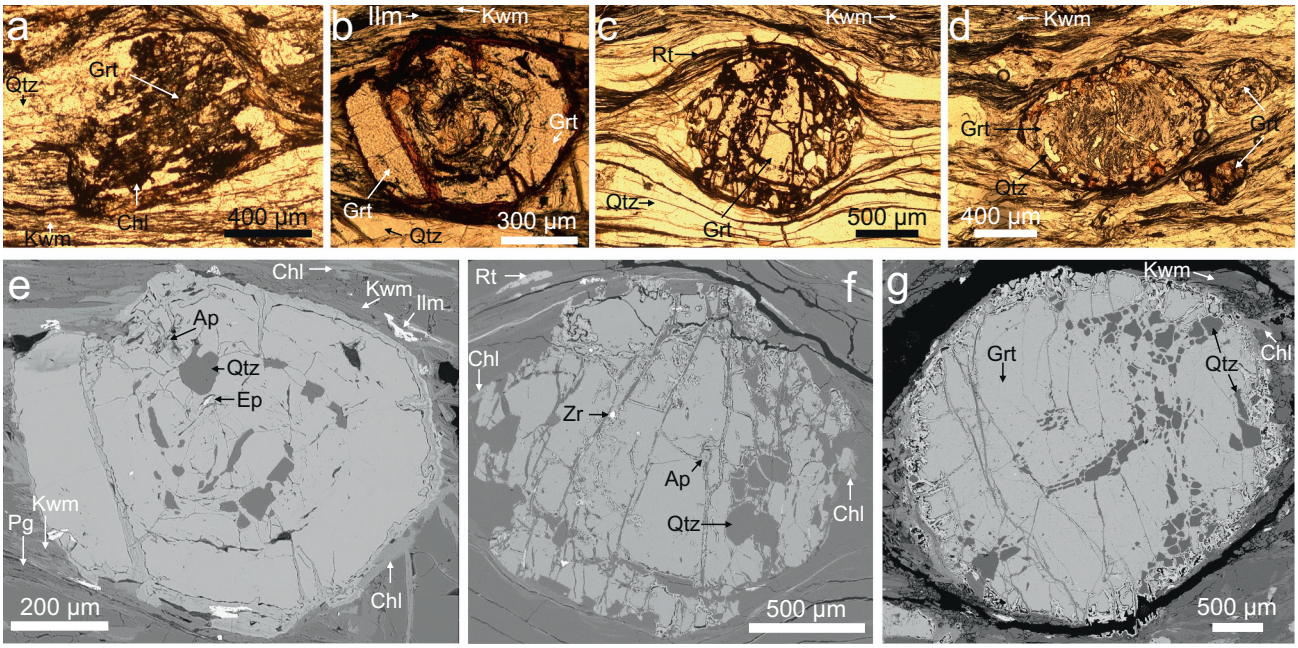

Fig. 3. Optical microscopy (**a**, **b**, **c**, **d**) and Backscatter electron images (BSE, **e**, **f**, **g**) of a garnet porphyroblast and the surrounding mineral matrix in the studied samples. Abbreviations: ap (apatite), chl (chlorite), ep (epidote), grt (garnet), ilm (ilmenite), pg (paragonite), Kwm (K-white mica), qtz (quartz), rt (rutile), zr (zircon).

metapelites attributed to the Ragua unit consisting of quartz, albite, K-white mica, paragonite, chlorite and garnet, and the accessory phases graphite, epidote, rutile, ilmenite, apatite, titanite and zircon. Most of the garnet porphyroblasts have been partially or completely replaced by chlorite. The preserved garnet grains are relatively small (< 1 mm), and they contain inclusions of quartz, ilmenite, epidote, zircon and titanite.

Sample 10.1 is a fine grained dark mica-schist (Fig. 3b, e) selected in the metaquartzites and metapelites alternations from the lower part of the Calar-Alto unit. The sample is made of quartz, K-white mica, paragonite, chlorite, chloritoid and garnet as main phases, and ilmenite, rutile, epidote and allanite as accessory phases. The size of the garnet porphyroblasts is up to 800 µm, and they show inclusions of quartz (mainly located in the core), graphite, ilmenite, epidote, allanite, zircon and titanite.

Sample RA-0 is a dark-grey mica-schist (Fig. 3c, f) which was selected in the mica-schists from the middle part of the Calar-Alto unit. This sample is formed by quartz, K-white mica, paragonite, chlorite, chloritoid and garnet, and the accessory phases apatite, zircon, rutile, tourmaline, ilmenite and monazite. Garnet porphyroblasts have a size of up to 1 mm and show fractures. The porphyroblasts are slightly deformed and contain numerous inclusions of quartz and in lower amount of graphite, rutile, zircon and apatite.

Sample 16.8 is a grey mica-schist (Fig. 3g) from the upper part of the Calar-Alto unit, showing major phases of quartz, albite, K-white mica, paragonite, chloritoid, chlorite and garnet and accessory phases of graphite, ilmenite, rutile, apatite, epidode, allanite, tourmaline and biotite. Garnet porphyroblasts have a size up to 3 mm. They are highly deformed and show numerous fractures. The inclusions in garnet are quartz, rutile, zircon, biotite and apatite.

Sample 16.16 is a dark grey mica-schist (Fig. 3d) selected in the uppermost levels of mica-schists in the Bédar-Macael unit, containing quartz, albite, K-white mica, paragonite, chloritoid, chlorite and garnet as major phases, and graphite, titanite, biotite, ilmenite, rutile, epidote, apatite and allanite as accessory phases. Garnet porphyroblasts have a size of up to 2 mm and inclusions of quartz, graphite, ilmenite, allanite, rutile and chlorite. Snowball and atoll garnets are commonly observed.

The mica-schists pertaining to the Calar-Alto and Bédar-Macael units (samples 10.1, RA-0, 16.8 and 16.16), are comparatively light-coloured than those from the Ragua unit (sample RA-0). Allanite was found in samples 16.8 and 16.16, with comparable features. Allanite size ranges between 40 and 160 µm and the grains are generally located in the mineral matrix. Few of them were observed as inclusion in the outer rim of garnet.

4.2. Microstructures

The studied samples exhibit either two planar fabrics S1 and S2 (samples RA-0, 10.1, 16.8, and 16.16), or a single foliation Sp corresponding to S2 (sample RA-2). For more detailed studies of the main fabrics in the Nevado-Filábride complex the reader is referred to the papers of Booth-Rea et al. (2015), Jabaloy et al. (2015) and Vera (2004).

The first cleavage S1 is parallel to the compositional layering and it was folded during formation of a crenulation cleavage defined as S2. In the sample RA-2 pertaining to the Ragua unit, S1 is not preserved. In the Calar-Alt unit, S1 is preserved in sample 10.1, in which K-white mica and paragonite (up to 100 µm long) form aggregates intergrown by graphite lamellas; in sample RA-0 with K-white mica (up to 300 µm), paragonite (up to 200 µm) and chlorite (up to 200 µm); and in sample 16.8 as shown by interbedded thin grains of K-white mica and paragonite (up to 300 µm). In the Bédar-Macael unit the sample 16.16 shows intergrowths of K-white mica (200 µm), paragonite (100 µm), chlorite (50 µm) and fine lamellas of graphite are observed. It has already been proposed that the S1 cleavage formed during the prograde history under greenschist facies conditions (e.g. Martínez-Martínez, 1986; de Jong and Bakker, 1991). Despite possible partial re-equilibrations at higher grade (e.g. Airaghi et al., 2017), local mineral assemblage described before for S1 (when it is visible) support the conclusion that it was formed under greenschist facies conditions.

In sample RA-2, S2 is underlined by thick aggregates of chlorite (up to 600 µm long), plagioclase (250 µm) and intergrowths of K-white mica and paragonite (200 µm). In the Calar-Alto unit, the following mineral phases are observed into S2: in sample 10.1, chlorite (500 µm), chloritoid (100 µm), K-white mica (400 µm) and paragonite (200 µm) showing graphite inclusions; in sample RA-0, K-white mica (up to

400 μm) included by graphite lamellas, paragonite (up to 200 μm), and chlorite (up to 300 μm); in sample 16.8 K-white mica (up to 800 μm), paragonite (up to 300 μm), plagioclase (up to 300 μm) and chlorite (up to 500 μm) which includes K-white mica. In the Bédar-Macael unit sample 16.16 S2 is marked by K-white mica (up to 400 μm), chlorite (up to 100 μm), and paragonite (up to 200 μm) include graphite lamellas. The crenulation-cleavage S2 has been proposed to have formed during exhumation and cooling (Martínez-Martínez, 1986; Platt and Behrmann, 1986; García-Dueñas et al., 1988; Augier et al., 2005b). The local mineral assemblages described above for S2 suggest that S2 developed under greenschist facies conditions in the three units.

Inclusion trails in garnet cores of samples 16.16 and 10.1 record the geometry of the S1 cleavage, whereas the porphyroblasts are deformed by S2 in sample 16.8. These observations suggest that garnet nucleated and grew significantly after S1 and before S2. In sample RA-0, garnet porphyroblasts are undeformed preventing the relative timing to be established, as it is for sample RA-2 in which garnet was replaced by chlorite.

5. Results

5.1. Compositional zoning of garnet

The compositional variability of garnet was characterized via quantitative compositional mapping. The maps of end-member fraction are shown in Fig. 5 for the sample 16.16 from the Bédar-Macael unit, Fig. 6 for samples 16.8, RA-0 and 10.1 from the Calar-Alto unit, and Fig. 7 for the sample RA-2 from Ragua unit. Several growth zones of garnet were defined for each sample based on the compositional zonations (delimited by dashed lines in Figs. 5–7). The limit of each growth zone was set using the grossular map as reference. Smother transitions in almandine and pyrope maps suggest that the original composition may have been locally affected by diffusion. As these effects are restricted to ~10–40 μm around the limit (see below), it is assumed in the following that the central part of each growth zone was not significantly modified by diffusion allowing the growth composition to be preserved (other examples at similar conditions are given in Chapman et al., 2011). The average composition of each growth zone was determined by integrating the pixel compositions of a domain, whose size varies between 330 and 7200 μm^2 depending on the thickness of the growth zone. These garnet domains were carefully selected, avoiding mixing pixels, mineral inclusions and contact between zones that could have been affected by diffusion. For comparison among samples, these average compositions were also plotted in a ternary diagram (Fig. 4).

Garnet porphyroblasts in sample 16.16 exhibit a core with typical growth zoning: X_{grs} and X_{sps} decrease outward, whereas X_{alm} and X_{prp}

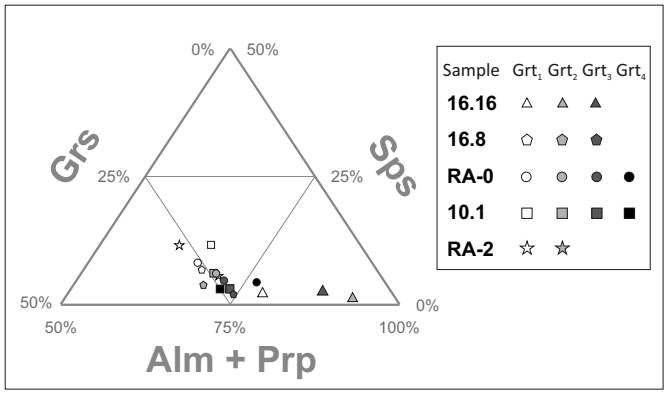

Fig. 4. Ternary compositional diagram of garnet: Grs (grossular fraction content), Sps (spessartine fraction content), Alm + Prp (almandine + pyrope fraction content).

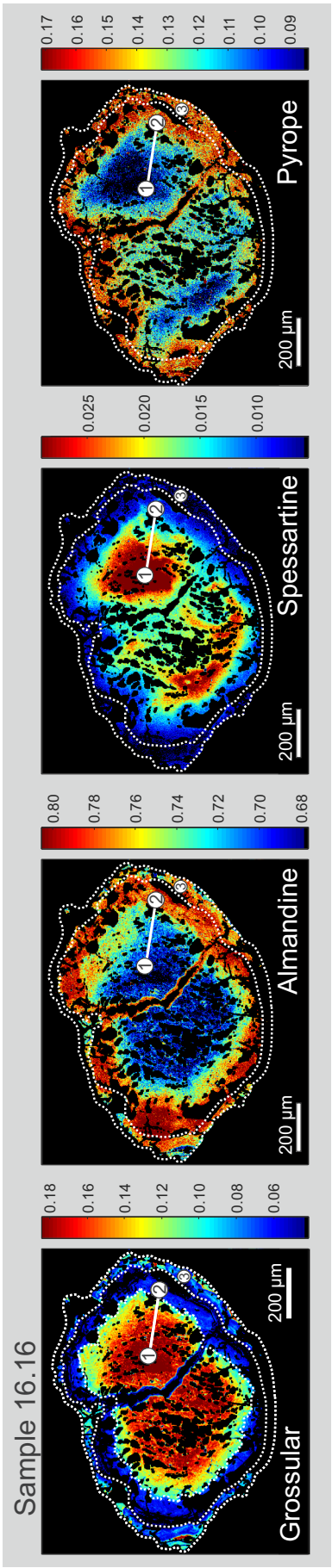

Fig. 5. Quantitative compositional maps of end-member fractions for a garnet porphyroblast of the Bédar-Macael unit (sample 16.16). Dashed lines delimit growth zones in garnet (see text). Circles show the location of the domains used for extracting the representative composition of each growth zone. Continuous lines show where compositional profiles reported in Supplementary Material S3 were obtained.

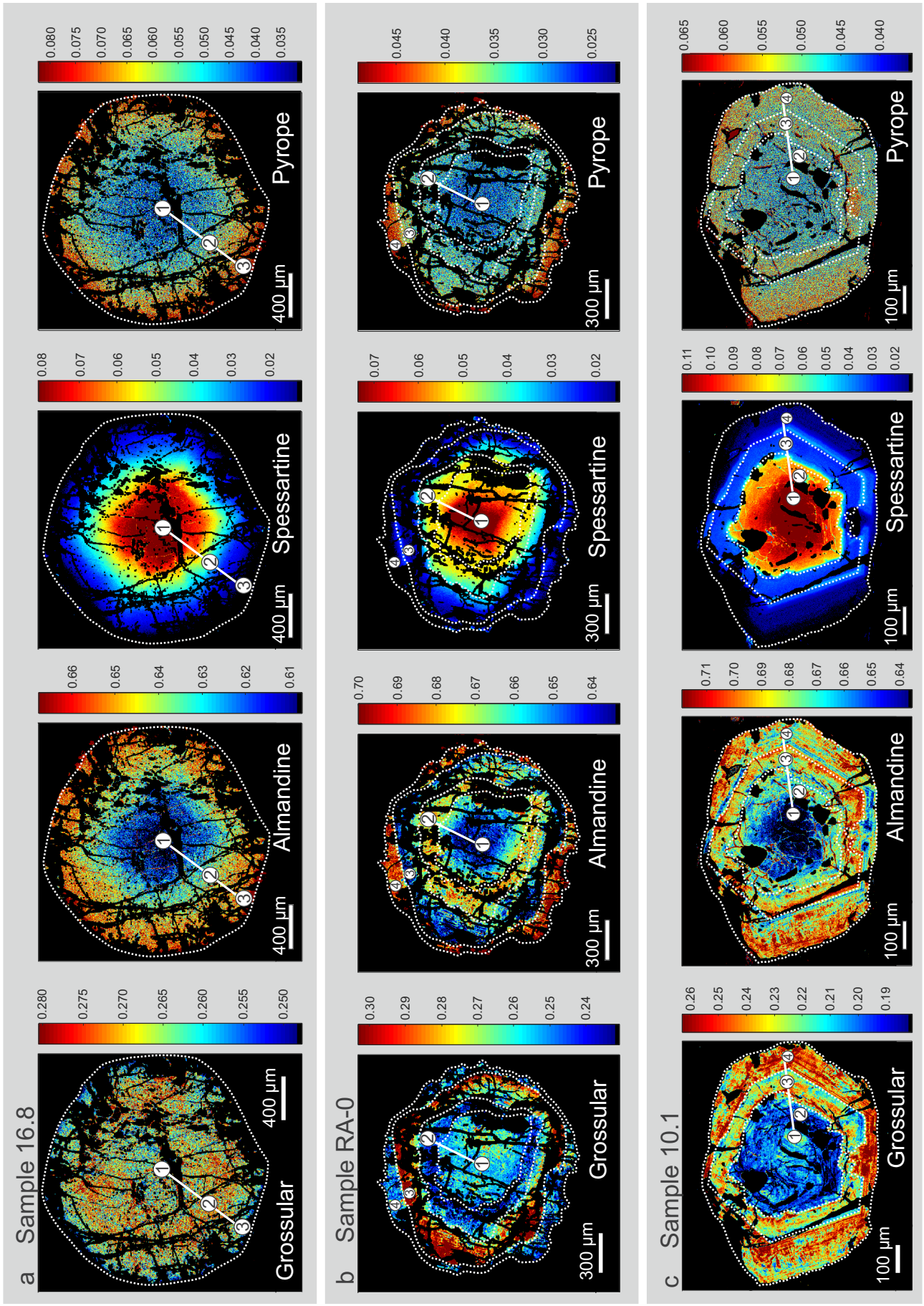

Fig. 6. Quantitative compositional maps of end-member fractions for garnet porphyroblasts of the Calar-Alto unit: **a** sample 16.8, **b** sample RA-0, **c** sample 10.1. Dashed lines delimit the successive growth zones in each garnet. Circles show the location of the domains used for extracting the representative composition of each growth zone. Continuous lines show where compositional profiles reported in Supplementary Material S3 were obtained.

both increase (Fig. 5). The core is surrounded by two narrow rims, which are not thicker than 100 µm and show lower X_{grs} and X_{sps} and higher X_{alm} and X_{prp}. A 50 µm thick fracture crosscuts the garnet core and is sealed by garnet with similar composition of the outermost rim (Fig. 5). Three garnet domains were selected in this sample. The first domain Grt_1 corresponds to the core of the porphyroblast. The average composition was obtained far away from the fracture (Fig. 5). Two additional garnet domains were selected, Grt_2 for the inner rim and Grt_3 for the outer rim and the fracture (Fig. 5).

Garnet in sample 16.8 does not exhibit significant variations in Ca, (0.87 ± 0.03 apfu) as shown by the X_{grs} map (Fig. 6a). By contrast, both X_{alm} and X_{prp} maps show lower values in the core (0.61 and 0.04) than in the rim (0.66 and 0.08). This chemical zonation is counterbalanced by a decrease of X_{sps} from 0.09 in the core to 0.01 in the rim. Three garnet domains were selected for modelling: the core Grt_1, the mantle Grt_2 and the rim Grt_3 (Fig. 6a).

Garnet porphyroblast in sample RA-0 shows a more complex zoning pattern including a core surrounded by three rings (Fig. 6b). The innermost ring is up to 300 µm thick, and the outermost is up to 150 µm. Garnet shows a oscillatory pattern in both X_{alm} and X_{grs}, with the core and the second ring enriched in X_{grs} and depleted in X_{alm}; the first and the outermost ring are both enriched in X_{alm}, and depleted in X_{grs}. By contrast, X_{prp} gently increases from core (0.03) to rim (0.05), whereas X_{sps} decreases (from 0.08 to 0.01). Based on the Ca map, four garnet domains were selected each corresponding to a single growth zone. Grt_1 was defined in the core, Grt_2 in the first ring, Grt_3 in the second ring and Grt_4 in the outermost rim (Fig. 6b). The sharp compositional transition between Grt_3 and Grt_4 in Ca, Fe and Mg support the assumption that post-growth intragranular diffusion was limited to a distance of < 10–40 µm.

Garnet porphyroblasts in sample 10.1 display three compositional domains delimited by roughly straight boundaries (Fig. 6c): a core surrounded by a mantle 50–80 µm thick, and a rim up to 160 µm thick. The core shows low X_{alm}, X_{grs} and X_{prp} (0.62, 0.22 and 0.05 respectively) and high X_{sps} (0.09–0.12). By contrast, the two other domains are enriched in X_{alm}, X_{grs} and X_{prp}, and depleted in X_{sps}. The Mn map shows small-scale diffusion between the core and the first rim, not larger than 15 µm (Fig. 6c). The slight manganese increase between the mantle and the rim from 0.02 to 0.05 suggests garnet resorption. This feature is only observed on the bottom side of the grain around a lobate structure generally interpreted as evidence of garnet resorption (e.g. Giuntoli et al., 2018). Two garnet domains were selected in the core for this sample, Grt_1 near the centre and Grt_2 in the outer part (Fig. 6c). Two additional garnet domains were chosen, Grt_3 for the mantle and Grt_4 for the rim (Fig. 6c).

Garnet porphyroblast from sample RA-2 are clustered of mineral inclusion making the zoning pattern more difficult to read and interpret. Nevertheless, several zones were identified including core surrounded by a thin rim (< 100 µm thick). The core shows a growth zoning where X_{grs} and X_{sps} decrease outward (from 0.03 to 0.02 and from 0.12 to 0.04 respectively), and X_{alm} and X_{prp} increase (from 0.59 to 0.69 and from 0.02 to 0.03). The rim is enriched in X_{alm}, X_{grs} and X_{prp} (0.67, 0.27, 0.03) and depleted in X_{sps} (0.04). Two garnet compositions were defined for this grain: a core Grt_1 and a rim Grt_2 (Fig. 7).

As shown in Figs. 6 and 7, samples 16.8, RA-0, 10.1 and RA-2 yielded similar compositional zoning between core and rim. Only garnet from sample 16.16 shows a separate trend characterized a remarkable enrichment in Fe toward the rim (Fig. 5).

As a summary, garnet porphyroblasts of every sample show typical growth zoning in core and mantle with limited post-growth modification by diffusion. These growth zones were thus selected and are used in the following to model the P-T conditions using equilibrium thermodynamics. By contrast, the garnet rims in samples 16.16 and RA-0 show more complex compositional zonation with oscillatory zoning. Although these features suggest non-equilibrium processes an attempt to model the rims with equilibrium thermodynamics is made in the

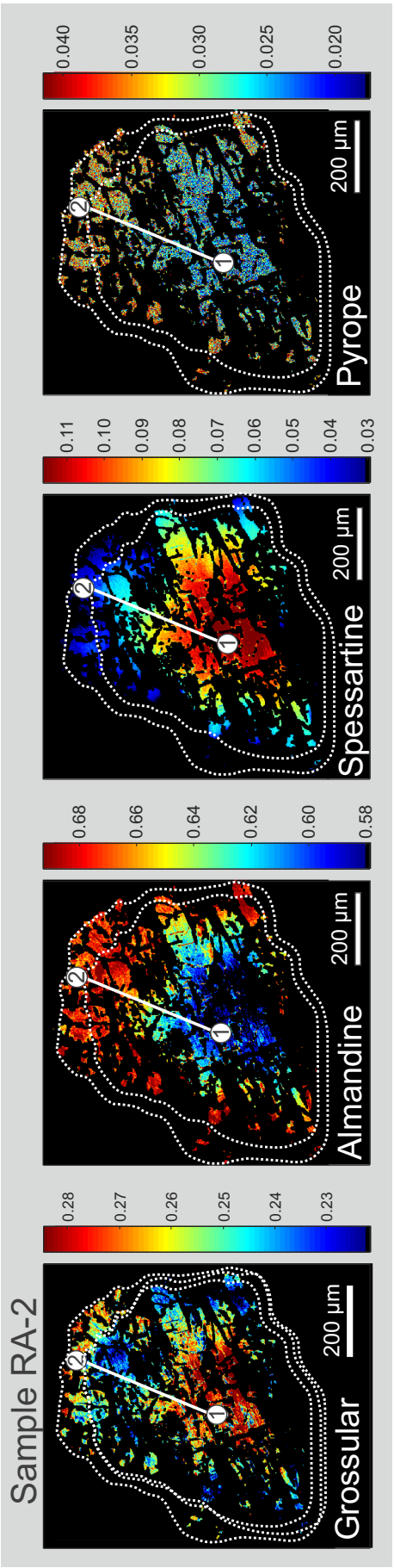

Fig. 7. Quantitative compositional maps of end-member fractions for a garnet porphyroblast of the Ragua unit (sample RA-2). Dashed lines delimit growth zones in the garnet. Circles show the location of the domains used for extracting the representative composition of each growth zone. Continuous lines show where compositional profiles reported in Supplementary Material S3 were obtained.

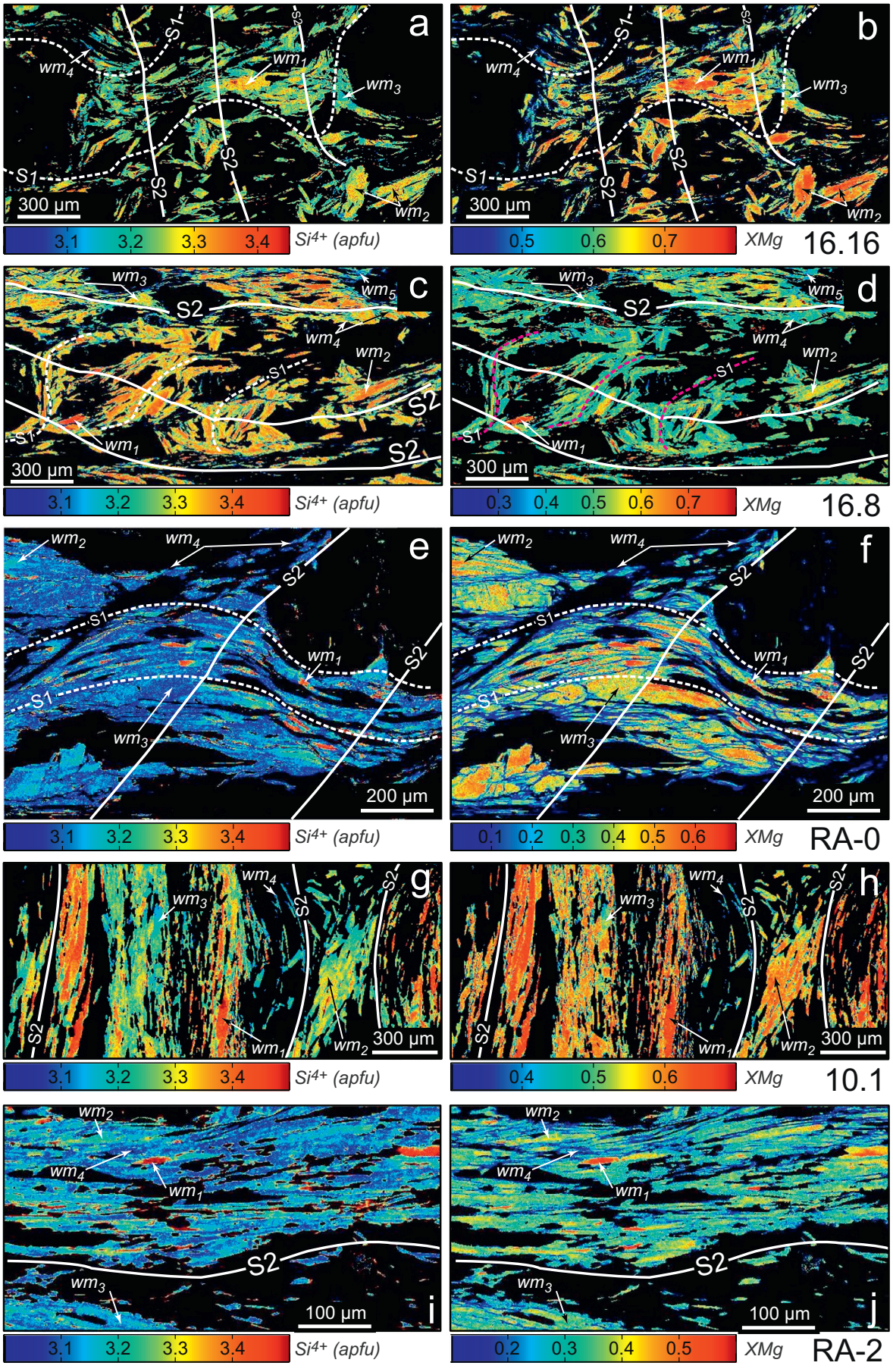

(caption on next page)

Fig. 8. Quantitative compositional maps of the Si content (atoms per formula unit, apfu) and XMg ($Mg/(Mg^{+}+Fe^{2+})$ assuming no ferric iron, $Fe^{3+}=0$) in K-white mica from samples 16.16 (**a**, **b**), 16.8 (**c**, **d**), RA-0 (**e**, **f**), 10.1 (**g**, **h**) and RA-2 (**i**, **j**).

following. The goal of this test is to determine if equilibrium thermodynamics remain a reasonable assumption (or if it does not).

5.2. Compositional zoning of K-white mica

The compositional variability of white mica was also characterized via quantitative compositional mapping. The Fig. 8 shows the compositional maps of Si^{4+} (unit apfu) and XMg for the five studied samples. As changes in Si^{4+} content and XMg are symptomatic of changes in pressure and temperature conditions (e.g. Massonne and Schreyer, 1987), different white mica compositional groups (wm_1, wm_2, etc.; see Fig. 8) were defined. It is important to notice that wm_1 systematically shows the higher Si^{4+} content – interpreted to reflect the higher-pressure conditions. The representative composition of each group is reported in Table 3. The structural formulae of white mica were calculated assuming all the iron to be Fe^{2+}. Compositional variables other than XMg are in apfu.

Four white mica compositional groups were defined in sample 16.16 (Fig. 8a, b). The higher values for the Si-XMg pair correspond to wm_1 (3.38 and 0.74), followed by wm_2 (3.29 and 0.72), wm_3 (3.18 and 0.53) and wm_4 (3.17 and 0.50). The compositions of wm_1 and wm_2 are preserved in the core of thick flakes (up to 400 μm long) preserved both in S1 and S2 (Fig. 8a, b); whilst lower values correspond to wm_4 fine lamellas. The Na content increases from 0.13 between wm_1 and wm_2 and up to 0.23 in wm_4.

In sample 16.8 (Fig. 8c, d), the values for the Si-XMg pairs progressively decrease for the five white mica compositional groups from 3.43 and 0.70 (wm_1), 3.31 and 0.65 (wm_2), 3.25 and 0.58 (wm_3), 3.18 and 0.48 (wm_4), down to 3.16 and 0.36 (wm_5). In both S1 and S2, the white mica flakes are up to 800 μm long and exhibits cores rich in Si^{4+} and XMg (wm_2 and wm_3), with depleted rims (wm_4) and scarce smaller grains pertaining to wm_5. The Na content varies between 0.032 in wm_1 up to a maximum of 0.309 in wm_4.

In sample RA-0 (Fig. 8e, f), high Si-content and XMg values were only observed in wm_1 (3.40 and 0.53). Lower values (in particular for the Si^{4+} content) were yielded by wm_2 (3.17 and 0.52), wm_3 (3.09 and 0.48) and wm_4 (3.00 and 0.07), which is a muscovite. This sample mainly preserves wm_2 and wm_3 as long grains aligned along S2. Scarce wm_1 (in grain cores) and wm_4 (as thin overgrowths) were observed (Fig. 8e, f). The Na-content increases between wm_1 and wm_3 (from 0.07 to 0.22), followed by a significant decrease in wm_4 (0.14).

Four white mica compositional groups were observed in sample 10.1 (Fig. 8g, h). In general both the Si-content and XMg values decrease from wm_1 (3.43 and 0.64), wm_2 (3.31 and 0.60), wm_3 (3.14 and 0.48), up to wm_4 (3.15 and 0.40). The groups wm_1, wm_2 and wm_3 form thick (150–200 μm) aggregates aligned along S2 (Fig. 8g, h). Few smaller grains of wm_4 are observed. The Na-content varies between the four groups increasing from 0.04 (wm_1) to 0.17 (wm_3), and then decreasing to 0.14 (wm_4).

The higher values of Si^{4+} content and XMg in sample RA-2 (Fig. 8i, j) correspond to a few grains of wm_1 (3.51 and 0.52). Remarkably lower values are recorded by wm_2 (3.21 and 0.38), wm_3 (3.11 and 0.35) and wm_4 (3.12 and 0.18). The white mica wm_2, wm_3 and wm_4 form remarkably long intergrowths aligned along S2, coating sparse wm_1 grains (Fig. 8i, j). A notable increase in the Na content is observed between wm_1 (0.06) and wm_4 (0.24).

5.3. Phase equilibria

Optimal P-T conditions for garnet were determined using iterative forward models and the program GrtMod (Lanari et al., 2017). A similar approach was followed for K-white mica using an in-house routine (see § 3.3). The results for all the studied samples are reported in Fig. 9. As the uncertainty envelopes are rarely symmetrical in both P and T for garnet, only the optimal solution is discussed in the following. Uncertainties are shown in Fig. 9 using the method proposed by Lanari et al. (2017) with a tolerance factor on C_o of 1.5.

Garnet nucleation is predicted at 518 °C and 1.8 GPa in sample 16.16 (Grt_1 in Fig. 9a); 489 °C and 1.7 GPa in sample 16.8 (Grt_1 in Fig. 8b); 511 °C and 0.8 GPa in sample RA-0 (Grt_1 in Fig. 8c); 488 °C and 1.8 GPa in 10.1 (Grt_1 in Fig. 8d); and 477 °C and 1.6 GPa in RA-2 (Grt_1 in Fig. 8e).

The results of garnet mantle and rims of each sample occur at lower P and higher T conditions compared to the conditions of garnet nucleation. In sample 16.16, Grt_2 (Fig. 9a) is predicted to have formed at 591 °C and 0.6 GPa, after 4.39 vol% of Grt_1 was fractionated from the reactive part of the rock. In sample 16.8, garnet mantle (Grt_2 in Fig. 9b) is predicted to have formed at 546 °C and 0.8 GPa (fractionation of 3.11 vol% of Grt_1); whilst garnet rim (Grt_3 in Fig. 9b) is modelled at 566 °C and 0.7 GPa (fractionation of 3.11 vol% and 3.66 vol% of Grt_1 and Grt_2 respectively). In sample RA-0 crystallization of Grt_2 (Fig. 9c) is modelled at 521 °C and 0.7 GPa (fractionation of 0.57 vol% of Grt_1). In sample 10.1, three additional domains of garnet were investigated: the outer core (Grt_2 in Fig. 9d) is modelled at 512 °C and 1.5 GPa (fractionation of 0.012 vol% of Grt_1) with large asymmetrical uncertainties in both temperature and pressure (Fig. 9d); the mantle (Grt_3) at 543 °C and 0.7 GPa (fractionation of 0.01 vol% of Grt_1 and 6.402 vol% of Grt_2) and the rim (Grt_4) at 548 °C and 0.7 GPa (fractionation of 0.01 vol% of Grt_1, 5.503 vol% of Grt_2, and 0.069 vol% of Grt_3). The garnet rim in sample RA-2 (Grt_2 in Fig. 9e) is modelled at 524 °C and 0.7 GPa (fractionation of 0.03 vol% of Grt_1).

In samples 16.16 and RA-0 some of the rims were not satisfactory modelled. In sample 16.16, the outer rim Grt_3 exhibits a complex oscillatory zoning (Fig. 5). The lower residual value of 0.082 (C_o) was found at 585 °C and 0.6 GPa. In sample RA-0, the inner and outer rims Grt_3 and Grt_4 also show complex compositional zoning (Fig. 6b). The lower residual values of 0.088 and 0.078 were found at 527 °C and 0.7 GPa for Grt_3, and 529 °C and 1.1 GPa for Grt_4.

White mica P-T conditions were assigned to three different groups: (1) relict of HP K-white mica (blue ellipses in Fig. 9); (2) K-white mica equilibrated during exhumation and heating up to the temperature peak (green ellipses in Fig. 9); and (3) K-white mica re-equilibrated during cooling (red ellipses in Fig. 9).

In sample 16.16, K-white mica reflect HP conditions of 1.4–1.9 GPa, and 450–520 °C (wm_1, wm_2 and wm_3, Fig. 9a); only a small fraction of K-white mica show lower pressure and higher pressure conditions of 0.7 GPa and ~580 °C (wm_4, Fig. 9a).

Sample 16.8 preserves K-white mica relics predicted to be stable at 1.8–2.3 GPa and 450–510 °C (wm_2 and wm_3, Fig. 9b); Note that wm_1 were not successfully modelled in the P-T window. A small fraction of K-white mica were equilibrated close to the temperature peak at 0.7–0.8 GPa and ~590 °C (wm_4, Fig. 9b) upon cooling at 0.4–0.7 GPa and 475–555 °C (wm_5, Fig. 9b).

Only a few K-white mica compositions suggest HP conditions in sample RA-0 (2.1–2.3 GPa and 450–490 °C; wm_1 in Fig. 9c), they otherwise recorded lower pressure and higher temperature conditions between 1.2 and 1.7 GPa (wm_2, Fig. 9c) and close to the temperature peak between 0.6 and 1.2 GPa (wm_3, Fig. 9c). Post temperature peak K-white mica forms a cluster at 0.4–0.6 GPa and 470–525 °C.

K-white mica in sample 10.1 shows mostly high-pressure conditions of 1.6–2.3 GPa and 450–520 °C (wm_1 and wm_2 in Fig. 9d). A few compositions suggest equilibration during exhumation at 0.6–1.4 GPa and 505–556 °C (wm_3, Fig. 9d), and during cooling at 0.4–0.8 GPa and 450–530 °C (wm_4, Fig. 9d).

Table 3
Representative mineral composition of K-white mica from the analysed samples. XMg = $Mg/(Mg^{2+}+Fe^{2+})$.

Sample	16.16				16.8					RA-0				10.1				RA2			
	wm_1	wm_2	wm_3	wm_4	wm_1	wm_2	wm_3	wm_4	wm_5	wm_1	wm_2	wm_3	wm_4	wm_1	wm_2	wm_3	wm_4	wm_1	wm_2	wm_3	wm_4
SiO_2	50.973	49.126	47.056	45.648	51.054	49.241	48.144	46.474	46.188	51.471	47.647	46.55	44.362	50.541	48.556	46.591	45.68	52.909	48.124	46.547	45.945
TiO_2	0.632	0.416	0.436	0.34	0.378	0.51	0.467	0.46	0.464	0.27	0.307	0.203	0.185	0.214	0.344	0.281	0.332	0.249	0.342	0.296	0.269
Al_2O_3	29.688	30.983	32.666	30.652	27.855	30.117	31.723	32.479	32.047	28.594	34.311	36.503	32.396	27.107	29.782	33.875	31.142	27.232	33.505	35.482	34.548
FeO	1.809	1.464	2.126	4.701	2.122	2.049	1.936	2.412	3.261	3.752	1.767	0.67	11.708	2.699	2.312	1.635	4.428	3.141	2.265	1.397	2.349
MnO	0	0	0	0	0	0	0	0	0	0	0	0	0	0	0	0	0	0	0	0	0
MgO	2.112	2.087	1.392	1.57	2.824	2.174	1.518	1.094	0.936	2.314	0.855	0.353	0.316	2.691	1.953	0.862	1.737	1.981	0.778	0.368	0.264
CaO	0.012	0.014	0.014	0.016	0.019	0.014	0.011	0.017	0.009	0.029	0.028	0.022	0.031	0.012	0.011	0.008	0.011	0.03	0.038	0.04	0.064
Na_2O	1.035	1.028	1.172	1.684	0.211	0.72	0.93	0.996	2.033	0.526	1.153	1.685	1.091	0.269	0.759	1.319	1.077	0.455	0.907	1.21	1.776
K_2O	9.094	9.436	9.323	7.832	9.665	9.483	9.351	9.355	8.425	8.908	8.95	8.723	7.894	10.043	9.749	9.51	8.992	8.788	8.844	9.012	7.965
Total	95.356	94.554	94.186	92.442	94.129	94.309	94.08	93.287	93.363	95.864	95.02	94.708	97.985	93.575	93.465	94.08	93.398	94.785	94.801	94.351	93.179
Si^4	3.38	3.287	3.18	3.174	3.429	3.314	3.246	3.176	3.161	3.404	3.166	3.085	3.004	3.433	3.308	3.143	3.151	3.514	3.207	3.113	3.121
Al (T2)	0.62	0.713	0.82	0.826	0.571	0.686	0.754	0.824	0.839	0.596	0.834	0.915	0.996	0.567	0.692	0.857	0.849	0.486	0.793	0.887	0.879
Si (T2)	1.38	1.287	1.18	1.174	1.429	1.314	1.246	1.176	1.161	1.404	1.166	1.085	1.004	1.433	1.308	1.143	1.151	1.514	1.207	1.113	1.121
V (M1)	0.992	0.979	0.96	0.89	0.963	0.964	0.971	0.96	0.975	0.93	0.965	0.99	0.705	0.971	0.976	0.985	0.885	0.984	0.959	0.976	0.965
Fe (M1)	0.011	0.006	0.011	0.08	0.011	0.012	0.012	0.024	0.019	0.034	0.024	0.005	0.283	0.01	0.009	0.007	0.067	0.008	0.025	0.017	0.03
Mg (M1)	0	0.015	0.028	0.031	0.026	0.024	0.017	0.016	0.007	0.036	0.011	0.005	0.012	0.019	0.015	0.008	0.048	0.009	0.015	0.007	0.006
Al (M2 M3)	1.699	1.731	1.779	1.676	1.635	1.703	1.767	1.791	1.743	1.634	1.853	1.938	1.576	1.603	1.695	1.836	1.682	1.646	1.838	1.908	1.872
Mg (M2 M3)	0.212	0.193	0.112	0.132	0.257	0.194	0.136	0.095	0.089	0.193	0.074	0.03	0.019	0.254	0.183	0.079	0.13	0.187	0.062	0.03	0.021
Fe (M2 M3)	0.088	0.076	0.109	0.192	0.109	0.103	0.097	0.113	0.167	0.174	0.073	0.032	0.405	0.143	0.122	0.085	0.188	0.167	0.101	0.061	0.106
XMg	0.739	0.717	0.526	0.497	0.702	0.653	0.581	0.477	0.357	0.528	0.521	0.479	0.067	0.638	0.597	0.478	0.398	0.529	0.381	0.348	0.183
XFe	0.261	0.283	0.474	0.503	0.298	0.347	0.419	0.523	0.643	0.472	0.479	0.521	0.933	0.362	0.403	0.522	0.602	0.471	0.619	0.652	0.817
K	0.77	0.805	0.805	0.695	0.829	0.814	0.805	0.816	0.736	0.752	0.759	0.738	0.682	0.87	0.847	0.818	0.792	0.745	0.751	0.769	0.692
V	0.096	0.06	0.04	0.071	0.138	0.09	0.072	0.049	0	0.179	0.091	0.044	0.172	0.093	0.052	0.009	0.063	0.194	0.128	0.071	0.069
Na	0.133	0.133	0.154	0.232	0.032	0.095	0.123	0.134	0.309	0.067	0.149	0.217	0.144	0.036	0.1	0.172	0.144	0.059	0.117	0.157	0.235
Sum	0.903	0.939	0.959	0.927	0.861	0.909	0.927	0.95	1.045	0.819	0.907	0.955	0.826	0.906	0.947	0.991	0.936	0.804	0.869	0.926	0.927
X_{cel}	0.298	0.259	0.201	0.26	0.341	0.278	0.221	0.191	0.222	0.321	0.137	0.061	0.255	0.377	0.292	0.158	0.254	0.343	0.151	0.088	0.12
X_{ms}	0.476	0.555	0.61	0.47	0.501	0.549	0.592	0.631	0.461	0.463	0.639	0.681	0.541	0.502	0.56	0.657	0.569	0.412	0.623	0.694	0.589
X_{prl}	0.093	0.058	0.046	0.078	0.128	0.084	0.071	0.054	0.048	0.156	0.084	0.045	0.108	0.088	0.053	0.019	0.058	0.187	0.117	0.068	0.072
X_{pg}	0.133	0.128	0.143	0.192	0.03	0.089	0.117	0.125	0.27	0.059	0.14	0.212	0.097	0.034	0.096	0.166	0.118	0.057	0.109	0.15	0.22

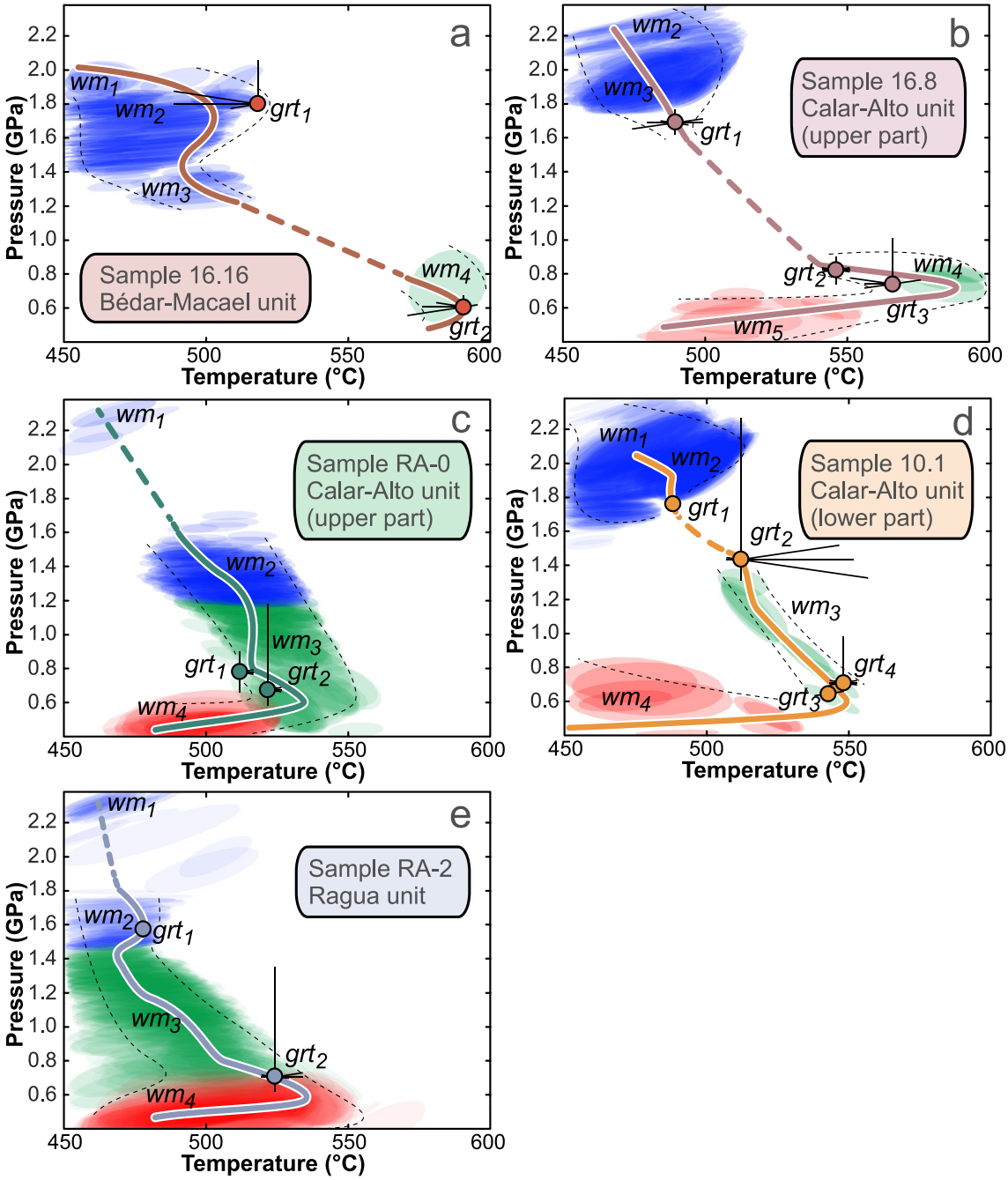

Fig. 9. P-T results and interpreted P-T paths for each sample: **a** sample 16.16, **b** sample 16.8, **c** sample RA-0, **d** sample 10.1, **e** sample RA-2. Uncertainties for garnet were determined using the method proposed by Lanari et al. (2017) with a tolerance factor on C_o of 1.5. The reference numbers correspond to the selected garnet domain. P-T estimates from K-white mica are presented as ellipses with an uncertainty of ± 0.01 for both Si and XMg.

In sample RA-2 the high-pressure K-white mica shows conditions of 2.2–2.4 GPa, 400–495 °C (wm_1 in Fig. 9e) and 1.5–1.8 GPa, 450–490 °C (wm_2). A large fraction of K-white mica compositions show lower pressure conditions between 0.6 and 1.4 GPa, and higher temperatures of 450–520 °C. Finally, a remarkable population of K-white mica equilibrated during cooling at conditions of 0.4–0.7 GPa and 455–550 °C.

As a summary, in most of the samples (except for RA-0), garnet nucleation is modelled at high-pressure conditions, above ~1.6 GPa and temperatures ranging between 480 and 525 °C (Fig. 9). This HP-LT stage is also largely recorded by K-white mica (blue ellipses in Fig. 9). Garnet in sample RA-0 apparently recorded nucleation at lower pressure conditions below 0.8 GPa at 511 °C (Fig. 9c). By contrast all the following growth stages of garnet, involving mantle and rims, yield lower pressure and slightly higher temperature conditions characteristic of a LP/HT stage. The behaviour of white mica upon exhumation and heating is more complex and sample dependent, but the results are systematically in line with the garnet conditions. Finally it was not possible to model with reasonable residuals the outer garnet rim(s) of samples 16.16 and RA-0.

5.4. Allanite dating

The dating results of allanite for samples 16.16 and 16.8 are summarized in Fig. 10 (see methods in § 3.5, and Burn et al., 2017). The data were plotted in (1) uncorrected Terra-Wasserburg diagrams to estimate the $^{207}Pb/^{206}Pb$ common lead composition; (2) Th-isochron

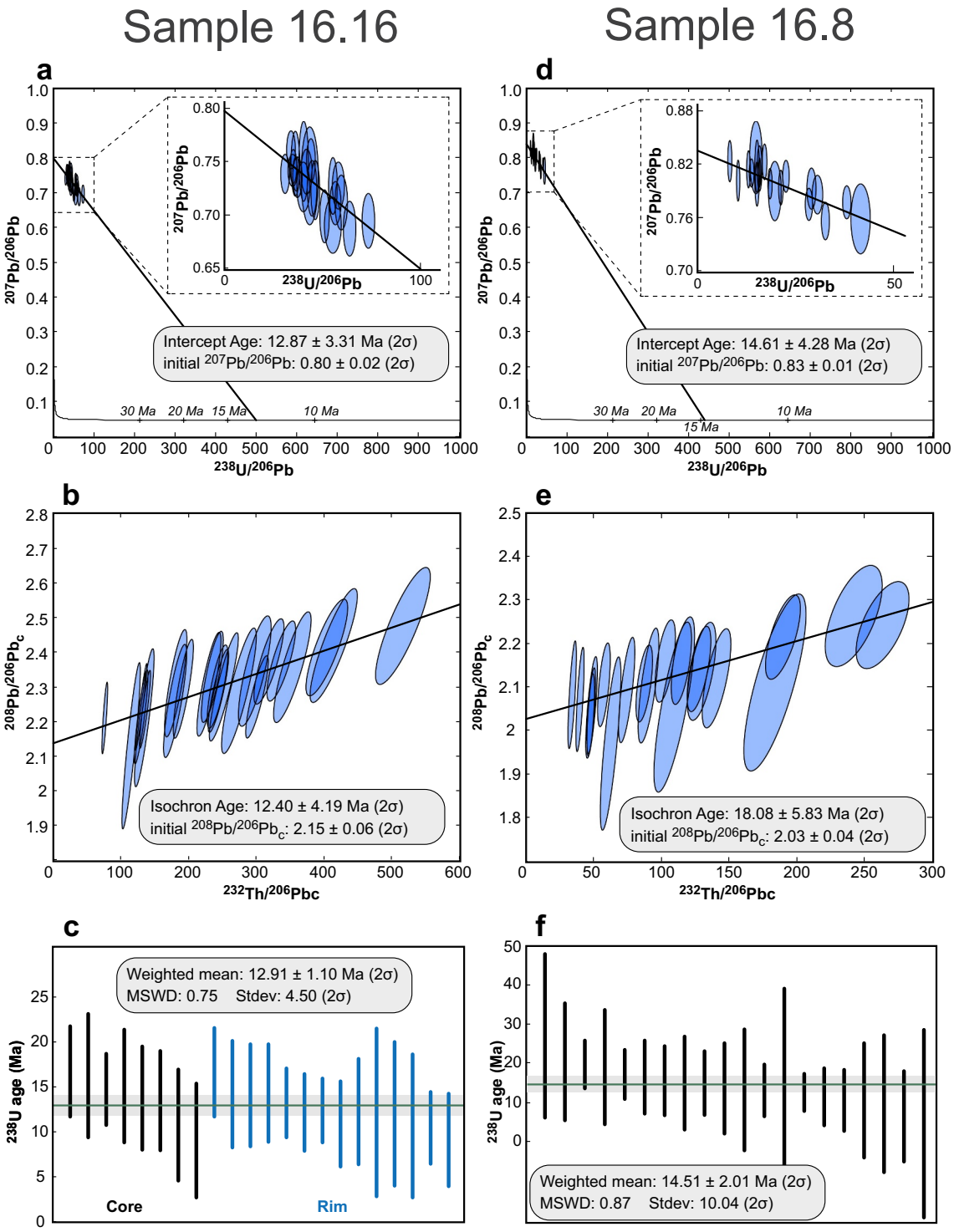

Fig. 10. LA-ICP-MS Th-U-Pb allanite dating results. The figure shows the Terra-Wasserburg and Th-isochron diagrams as well as the weighted mean U–Pb age for samples 16.16 (**a**, **b**, **c**) and 16.8 (**d**, **e**, **f**).

diagrams, in which the uncertainty on the common lead fraction (f_{206}) was propagated through the age calculation procedure using a Monte-Carlo technique (Burn et al., 2017); and as (3) common lead corrected U ages using the common lead compositions from (1) and (2).

In sample 16.16, the U- and Th- isochrons defined by 21 allanite analyses yield the intercept ages of 12.87 ± 3.31 Ma (2σ, Fig. 10a) and 12.40 ± 4.19 Ma (2σ, Fig. 10b). The corresponding weighted mean U—Pb age is of 12.91 ± 1.10 Ma (2σ). Allanite core and rim analyses returns the same age within uncertainty (MSWD = 0.75, see Fig. 10c).

In sample 16.8, the U- and Th- isochrons defined by 20 allanite analyses yield the intercept ages of 14.61 ± 4.28 Ma (2σ, Fig. 10d), and 18.08 ± 5.83 Ma (2σ, Fig. 10e). The corresponding weighted mean U—Pb age is of 14.51 ± 2.01 Ma (2σ, Fig. 10f).

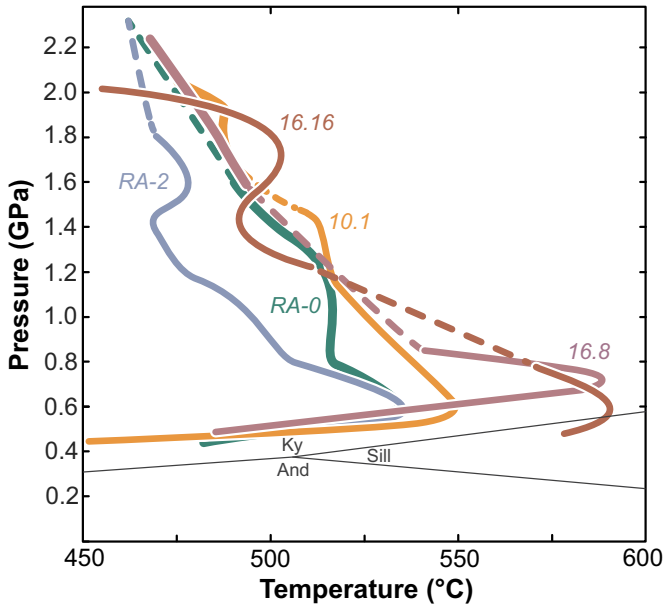

Fig. 11. Synthetic P-T diagram showing the P-T paths obtained in this study (see details in Fig. 9).

6. Discussion

6.1. Phase equilibria modelling

In this study, garnet and K-white mica were modelled using Gibbs free energy minimization and an iterative approach. The predicted mineral assemblages for the HP stage were not considered to refine the P-T conditions which only rely on the garnet and white mica compositions.

6.1.1. Garnet

This technique applied to model garnet cores (Grt_1) is similar in essence to isopleth thermometry without considering the coexisting assemblage. The main advantages of GrtMod are (1) to enable garnet fractionation and (2) resorption in order to compute a suitable reactive bulk composition at each stage and (3) the weighting procedure included in the inversion (Lanari et al., 2017), allowing "optimal" P-T conditions to be derived in a quantitative way (see Fig. 11 in Lanari and Duesterhoeft, 2019 for a comparison between the weighted and unweighted procedure).

The robustness of the model predictions, such as the garnet compositions and the volume fractions, was tested along a profile (the positions are shown in Figs. 5–7). The results are given in Supplementary Material S3. The chemical composition of garnet was extracted using XMapTools. The distances between each pixel was transformed into a volume fraction of garnet assuming a total of 4.89 vol% (sample 16.16), 11.07 vol% (sample 16.8), 1.74 vol% (sample RA-0), 11.89 vol% (sample 10.1) and 0.71 vol% (sample RA-2) of garnet being produced. The modelled garnet modes are in line with the observations in each sample. This procedure allows the zoning profiles and predictions to be compared assuming a single-size population of garnet (e.g. Lanari et al., 2017). The modelled garnet zoning profiles are consistent with the observation for most samples (S2), suggesting an overall good quality of the models. Minor discrepancies are caused by chemical variations within a single growth zone due to Rayleigh fractionation (e.g. core in sample 16.16) or by small oscillations in chemical composition within a single growth zone (e.g. rim in sample 10.1). These were probably controlled by kinetics rather than chemical equilibrium and cannot be modelled using Gibbs free energy minimizations relying on the assumption of chemical equilibrium.

As presented in Section 5.3, the outer rims of garnet in samples 16.16 and RA-0 yielded high residual values. The observed garnet compositions cannot be modelled with our model based on equilibrium thermodynamics; these are interpreted to reflect disequilibrium processes such as transport-controlled growth and they are excluded from the comparison shown above.

6.1.2. K-white mica

Mineral fractionation and resorption were not considered for white mica modelling as this is known to have little effects on the position of the Si^{4+} and XMg isopleths (Airaghi et al., 2017). K-white mica records a similar trend in all the studied samples with the preservation of a HP generation and partial re-equilibration during exhumation and heating, eventually followed by new growth upon cooling (Fig. 9). The HP generation is observed as cores (e.g. samples 16.16, RA-0 and 10.1) or single-grains (e.g. samples 16.8 and RA2) that are preserved in S2 and S1 (if present, see Fig. 8). This observation shows that white mica re-equilibration occurs by dissolution-precipitation and that the composition cannot be related to D1 and D2 deformations stages. Similar conclusions were reached for amphibolite facies metapelites in the Longmen Shan (Airaghi et al., 2017; Airaghi et al., 2019). The degree of re-equilibration is likely controlled by the availability of fluids driving pseudomorphic replacement (Putnis, 2009; Airaghi et al., 2017; Berger et al., 2017). In the present study, white mica from samples RA-0 and RA-2 were strongly re-equilibrated compared to white mica in samples 16.16, 16.8 and 10.1 that preserve a higher fraction of HP mica. This study shows that the interpretation of white mica thermobarometry in link with deformation can be erroneous if not assisted by quantitative compositional maps.

6.2. Comparison between units

The combination of thermobarometric results obtained for garnet and K-white mica allows the P-T paths of each sample to be reconstructed (Fig. 11). The absolute uncertainty on any P-T estimate is commonly assumed to be close to ± 50 °C and ± 0.2 GPa. However, as the same modelling technique and thermodynamic properties are used, the relative uncertainty is assumed to be much smaller (between 10 and 25 °C, see the uncertainty envelopes in Fig. 9) permitting to perform relative thermobarometry (e.g. Worley and Powell, 2000).

The studied samples exhibit clockwise P-T paths characterized by a HP/LT stage followed by heating during decompression toward a LP/HT stage. The burial conditions however cannot be reconstructed as no relic was found. For the HP/LT stage, a small difference of 0.2 GPa is observed between samples 16.8, RA-0 (Calar-Alto unit) and RA-2 (Ragua unit) (~2.3 GPa), and samples 16.16 (Bédar-Macael unit) and 10.1 (Calar-Alto unit) (~2 GPa). The samples reached mostly the same temperature during the HP/LT stage (~465 °C in 16.8, RA-0 and RA-2; ~455 °C in 16.16; ~475 °C in 10.1). These differences can be related to the uncertainty in the thermodynamic model to predict the conditions of the Si^{4+} rich cores. Minor differences of < 30 °C are observed between the P-T path during the exhumation and heating stage. Samples 16.16 and 16.8 recorded a higher peak temperature of ~585 °C; this is not recorded by samples RA-0, 10.1 and RA-2 (~535–550 °C). Finally, following the LP/HT stage all samples show a similar cooling trajectory.

It is interesting to note that, despite stark differences in the thermal peak conditions between samples 16.16 (Bédar-Macael unit), 16.8, RA-0 and 10.1 (Calar-Alto unit), the pre-peak P-T trajectories are similar, including for the HP stage. Only sample RA-2 (Ragua unit) evolved at slightly lower temperature during exhumation, but this difference cannot be interpreted as statistically different given the range of uncertainty (see above).

The similarities in the P-T conditions during HP/LT stage and during decompression suggest that the units underwent a similar heating and exhumation history. By contrast, during the LP/HT stage, the temperature was higher in the upper part of the complex (samples 16.16

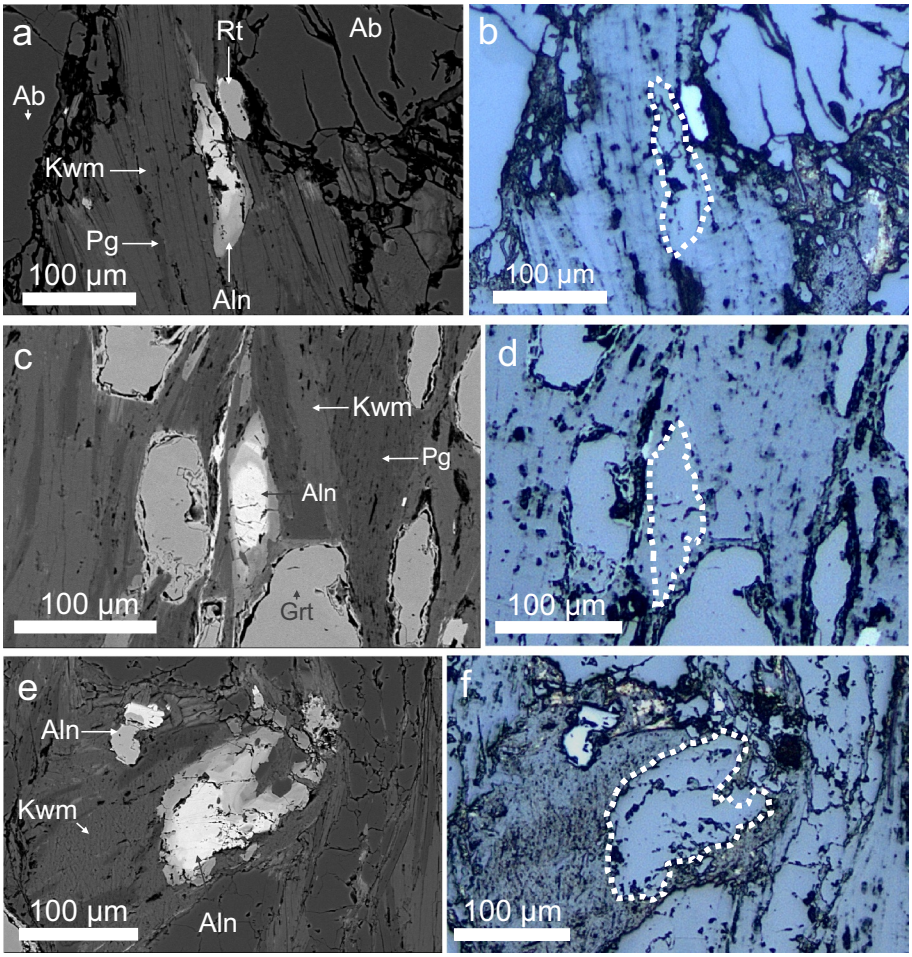

Fig. 12. BSE images (**a**, **c**, **e**) and optical microscopy microphotographs (**b**, **d**, **f**,) of allanite grains from samples 16.16 and 16.8 matrix. Abbreviations: ab (albite), aln (allanite), grt (garnet), pg (paragonite), Kwm (K-white mica), qtz (quartz), rt (rutile).

and 16.8) compared to the lower part (samples 10.1, RA-0 and RA-2). This result suggests that this inverted metamorphism observed in the Nevado-Filábride complex was recorded during collision. Other studies found higher P-T conditions for this stage in the upper part of the complex than in the lower one (e.g. Augier et al., 2005a, 2005b; Puga et al., 2000; Behr and Platt, 2012; Booth-Rea et al., 2015) but such features were not visible in our dataset.

6.3. Petrochronology

Allanite dating can provide age constraints of single metamorphic stage(s), provided that growth episodes can be correlated to major phases (Rubatto et al., 2011; Cenki-Tok et al., 2014; Loury et al., 2016; Engi, 2017). In this study, allanite from samples 16.16 and 16.8, pertaining to the Bédar-Macael and Calar-Alto units respectively, crystallized during Miocene at 12.91 ± 1.10 Ma and 14.51 ± 2.01 Ma respectively (Fig. 10c, f). In these two samples, allanite is present in the matrix (Fig. 12) and as inclusion in the outer rim of garnet (Fig. 13). No age difference was found between these two locations or between the REE-rich core and the REE-depleted rim of single grains (Fig. 12c). In both samples, allanite inclusions were found in the garnet rim (Fig. 13a) as well as along late fractures cross-cutting the previous growth zones. In Sample 16.16, allanite was found only in the outer rim (Grt_3) showing oscillatory zoning. These observations show that allanite formed before or syn Grt_3 and allanite dating provides a maximum age for the formation of the garnet rim in these samples. These rims correspond to the garnet domains that were not modelled using a chemical equilibrium model, i.e. Grt_3 in sample 16.16 (see § 5.3). The textural relationships and the potential presence of reactive fluids to form the last garnet rims in these samples suggest that the allanite formed during the LP/HT stage at ca. 13 Ma. Accordingly, the HP/LT stage should take place earlier as proposed by Augier et al. (2005a). Li and Massonne (2018) recognized two monazite populations formed at 40.2 ± 1.7 and 24.1 ± 0.8 Ma. According to these authors, a first HP event took place before the first monazite population formed, whereas the exhumation and a second P-T loop coincide with the age of the younger population. These stages are all older than the LP/HT stage recorded by allanite. The allanite dating results are also in line with Monié et al. (1991) that suggested an early Miocene HP stage. Other studies reported HP metamorphism occurring between 18 and 13 Ma (López-Sánchez-Vizcaíno et al., 2001; Platt et al., 2006; Gómez-Pugnaire et al., 2012; Kirchner et al., 2016) previous or nearly coincident with the allanite data for the LP/HT stage. The results of de Jong (2003), ~14 and ~17 Ma for the early stages of exhumation are previous or nearly coincident with the allanite data.

6.4. Comparison with literature data

The P-T trajectories obtained in this study are compared in the following sections with the P-T paths proposed in previous studies (Fig. 14).

6.4.1. Ragua unit

Augier et al. (2005b) proposed a clockwise P-T path for the Ragua unit (Fig. 14a). These conditions are similar to sample RA-2 except for wm_1 that indicates higher-pressure conditions (Fig. 9e). As only a few

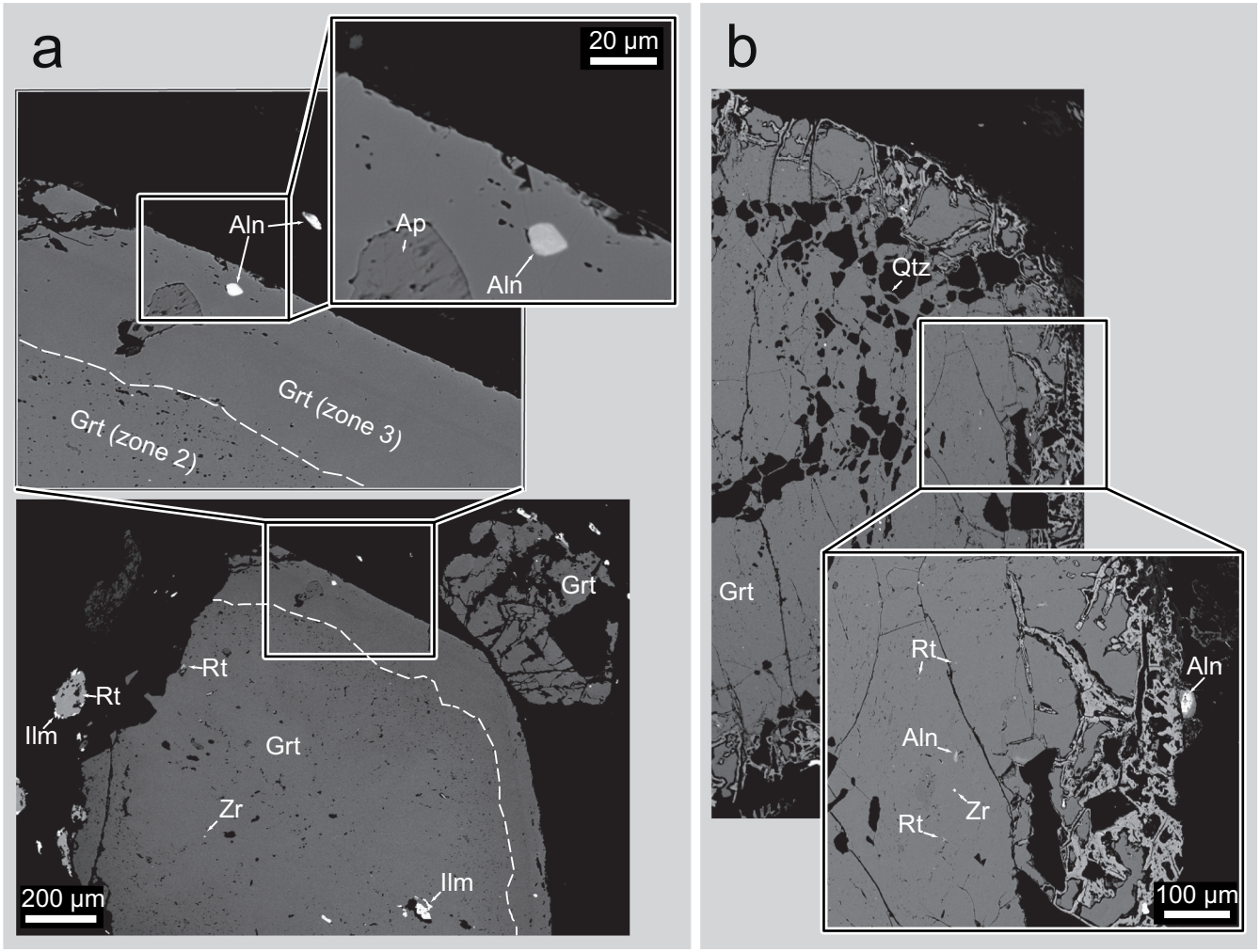

Fig. 13. BSE images of allanite inclusions in garnet porphyroblasts from samples 16.16 (**a**) and 16.8 (**b**). Abbreviations: aln (allanite), ap (apatite), grt (garnet), ilm (ilmenite), qtz (quartz), rt (rutile), zr (zircon).

grains aligned along S2 recorded these conditions, they are easy to miss without the assistance of compositional maps. For the LP/HT stage, the temperature reached by sample RA-2 is slightly higher (~25 °C) that proposed by Augier et al. (2005b) but this remain within the absolute uncertainty of each method. Li and Massonne (2018) proposed a different P-T path consisting of two successive hairpin P-T loops (path 2 in Fig. 14a); such pressure cycling is not recorded by white mica in our dataset. The authors interpreted the second loop as a consequence of overlying the hot Alpujárride complex. In all the samples investigated using quantitative compositional mapping, neither garnet, nor white mica recorded such complex P-T path involving two burial stages (see Rubatto et al., 2011 and Regis et al., 2014 for other examples of white mica zoning recording pressure cycling).

6.4.2. Calar-Alto unit

The results of Augier et al. (2005b) for the Calar-Alto unit show an isothermal decompression at ~550 °C (Fig. 14b). Our white mica data from samples RA-0, 10.1 and 16.8 rather suggest a non-isothermal decompression between ca. 2 and 0.6 GPa associated with a temperature rise of ~100 °C. The LP/HT stage of sample 16.8 is predicted to occur at temperatures 50 °C higher than Augier et al., (2005b) as already proposed by Li and Massonne (2018). Such reheating event of 60 °C as proposed by Li and Massonne (2018) is only observed in sample 16.8 and not associated to a second burial stage (Fig. 14b).

6.4.3. Bédar-Macael unit

In contrast with the two other units, the Bédar-Macael unit apparently recorded a large variety of P-T paths spreading over the entire P-T range. Bakker et al. (1989), Vissers et al. (1995) and Gómez-Pugnaire and Fernández-Soler (1987) (Fig. 14c) yielded values for the HP/LT between 0.5 and 0.7 GPa, significantly lower than the estimates from our garnet and white mica modelling in sample 16.16. However the continuous heating during exhumation observed in these P-T paths is in line with our results. The P-T estimates of Augier et al. (2005a) and Ruiz-Cruz et al. (2015) (Fig. 14c) have similar pressure conditions for the HP/LT stage (~1.9 GPa) but at significant higher temperature conditions (~600 °C). Behr and Platt (2012) and Puga et al. (2002) (Fig. 14c) proposed hairpin P-T trajectories with peak conditions of 550 °C, 1.4 GPa and 650 °C, 2.1 GPa respectively. In both cases decompression occurs together with cooling. Finally, higher temperature conditions were obtained by López-Sánchez-Vizcaíno et al. (2001) from ultramafic rocks (Fig. 14c). Such high-temperatures conditions are not compatible with the absence of partial melting in the metasediments of this area.

Despite the variety of P-T paths reported in the literature, our P-T data for both white mica and garnet in sample 16.16 indicate conditions similar to the other units (Fig. 11). Even though a higher internal degree of complexity cannot be excluded for the Bédar-Macael unit, our new dataset suggests a very similar metamorphic history for both the HP/LT and LP/HT stages.

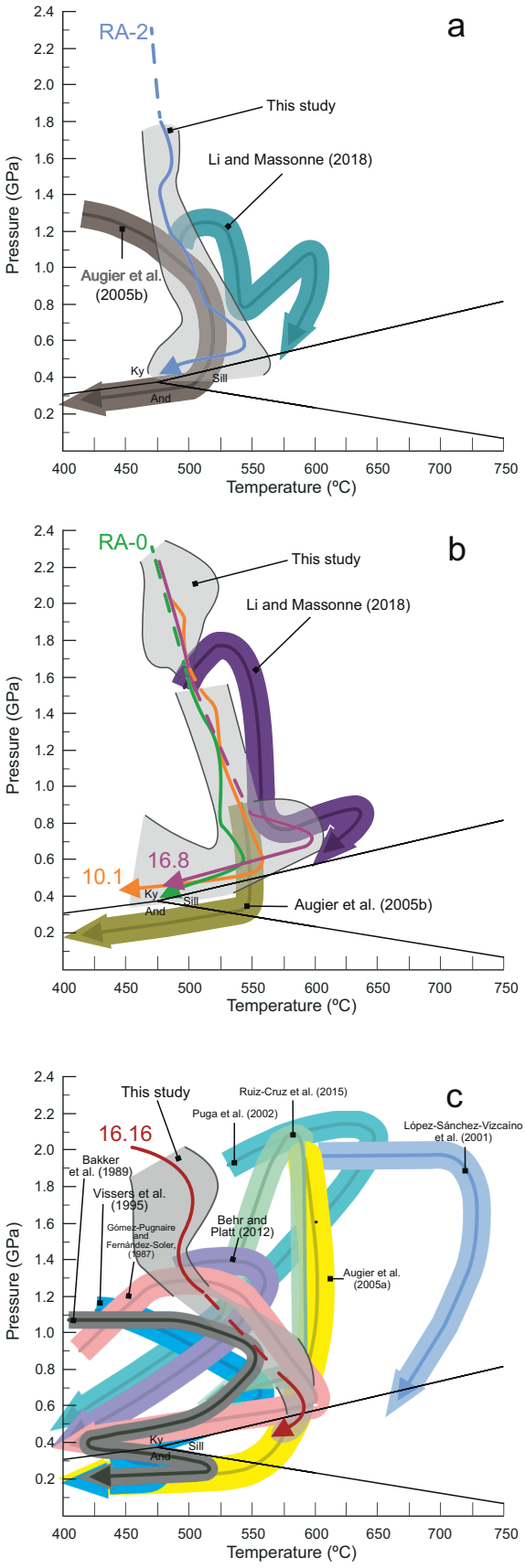

Fig. 14. Comparison between the P-T paths obtained in the present study and those available in the literature for: **a** Ragua unit, 1, **b** Calar-Alto unit, **c** Bédar-Macael unit.

Following the LP/HT stage, the retrograde stage follows a linear cooling trajectory. Other proposed P-T paths enter the field of andalusite and/or sillimanite (Augier et al., 2005b, Fig. 14a, b; Bakker et al., 1989; Vissers et al., 1995; Augier et al., 2005a, Fig. 14c) during decompression. However, kyanite is the only Alpine-age aluminosilicate reported in the Nevado-Filábride complex (e.g. Behr and Platt, 2012). With the exception of the sample 16.16, the trajectories presented in this study remain inside the kyanite stability field (Fig. 11).

6.4.4. *Summary*

The present study brings a new dataset for the Ragua unit, confirming the HP metamorphism proposed by Augier et al. (2005b) and Li and Massonne (2018). However, our data support similar peak-pressure conditions in the three units. The studied samples recorded a similar exhumation path associated to heating (Fig. 11). The thermal peak was recorded at similar depths of ~20 km but with a thermal gradient of 50 °C. This later stage was dated at 13–15 Ma. A higher degree of complexity in the Bédar-Macael unit – maybe involving several subunits with contrasted tectono-metamorphic histories – cannot be excluded from the literature data (see above).

6.5. *Tectonic implications*

The results of this study suggest that the three units followed similar exhumation trajectories. These results question the tectonic model of two independent complexes proposed by Puga et al. (2002). Despite the similarities in the P-T shapes, the uppermost rocks of the Nevado-Filábride record higher temperature conditions that the lowermost ones during the LP/HT stage. This difference has been attributed to various factors including: the existence of different tectono-metamorphic units or complexes (e.g. Puga et al., 2002); the proximity of the top to a hot hanging wall (e.g. Behr and Platt, 2012); a late-stage thermal overprint (Bakker et al., 1989) involving either shear heating or hot fluid flows

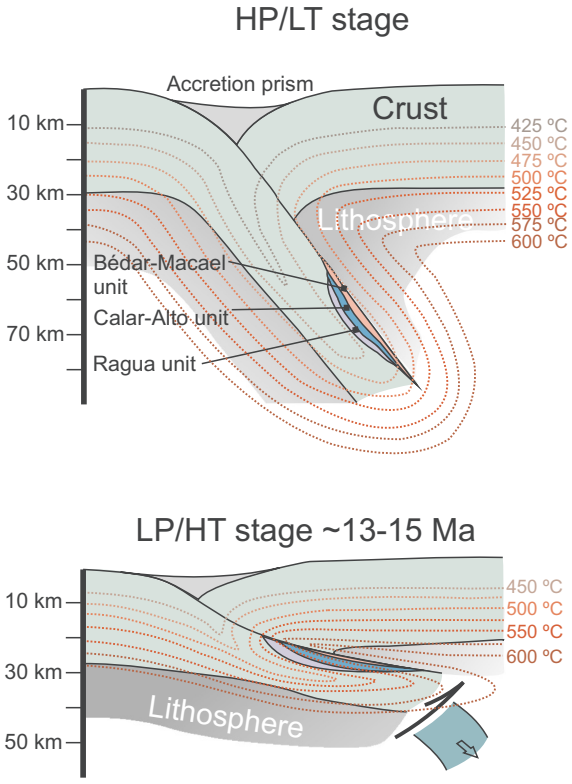

Fig. 15. Simplified model showing the evolution of the Nevado-Filábride complex during subduction and exhumation. According to the allanite data, exhumation should have started before ~13 Ma.

(Aerden et al., 2013); the upwelling of hot mantle material followed by magmatism (de Jong, 2003). The increase of the maximum temperature conditions toward the top of the series can be explained by the proximity with the mantle wedge (Fig. 15). The linear cooling after the LP/HT stage (Fig. 11) probably coincides with the final emplacement of the Nevado-Filábride complex underneath the Alpujárride complex.

Regarding the age of metamorphism, allanite dating from samples 16.16 (12.91 ± 1.10 Ma) and 16.8 (14.51 ± 2.01 Ma) allowed us to constrain the timing of the LP/HT stage at ca. 13–15 Ma. Cooling rate for retrograde metamorphisms estimated at ~120 °C/Ma, in line with the results of Johnson et al. (1997) of 105–200 °C/Ma. The peak-metamorphism age obtained from allanite is compatible with the existing time frame for the HP stage of 20–13 Ma (e.g. López-Sánchez-Vizcaíno et al., 2001; Gómez-Pugnaire et al., 2012; Platt et al., 2006; Kirchner et al., 2016), and 48–30 Ma (Monié et al., 1991; Augier et al., 2005a; Li and Massonne, 2018). A Miocene age for the HP/LT stage implies a rapid exhumation of the Nevado-Filábride complex as previously proposed (e.g., López-Sánchez-Vizcaíno et al., 2001; de Jong, 2003; Platt et al., 2006; Behr and Platt, 2012; Kirchner et al., 2016), and rapid exhumation rates of ~12 km/Ma. By contrast, the scenario of an Eocene HP/LT stage involves exhumation rate of 2.4–4.0 km/Ma. Rapid exhumation and cooling rates have also been proposed for the Western and Central Mediterranean region such as 20–24 km/Ma (Gebauer et al., 1997) and 36 km/Ma in Dora Maira Massif (Rubatto and Hermann, 2001); 6–8 km/Ma for the Edough massif (Northern Africa, Carminati et al., 1998); and 25 km/Ma for the Beigua Unit (Western Alps, Rubatto and Scambelluri, 2003). In addition, such rapid exhumation rates have also been proposed for the overlying Alpujárride complex (e.g. Platt et al., 2005; Platt et al., 2013) together with high cooling rates (350 °C/Ma, Lonergan and Johnson, 1998; 400 °C/Ma, Esteban et al., 2004; ~500 °C/Ma, Zeck, 2004).

Finally, our results question the existence of several tectono-metamorphic units and major discontinuities in the Nevado-Filábride complex. It cannot be excluded that the ductile to ductile-brittle shear zones observed throughout the complex are local discontinuities rather than crustal scale shear zones with km-scale displacements, which would have resulted in the superposition of rocks with different metamorphic histories. In this sense, the similarity of the P-T paths is interpreted here as a similar tectono-metamorphic history even though the units could have been subducted and exhumed sequentially. The similar age range of the LP/HT stage in the Bédar-Macael (sample 16.16) and the upper part of the Calar-Alto (sample 16.8) units also support this conclusion of a similar P-T-t history.

7. Conclusions

Five garnet-bearing mica-schists have been studied to obtain detailed P-T paths for the Alpine metamorphism followed by the Nevado-Filábride complex. The most notable findings in this study are:

- This study confirms the Nevado-Filábride complex recorded an apparent inverted metamorphism, characterized by higher P-T conditions in the upper part.
- The samples pertaining to the previously proposed Ragua, Calar-Alto and Bédar-Macael units followed clockwise P-T trajectories, both characterized by a first HP/LT stage, followed by heating during decompression leading to the LP/HT stage. The final part of the exhumation took place along a nearly linear cooling following the LP/HT stage.
- During the HP/LT stage, the Bédar-Macael unit reached ~2 GPa and ~520 °C. The temperature difference increased during the decompression up to ~70 °C during the LP/HT stage.
- The HP/LT stage in the Calar-Alto unit reached ~2.0–2.2 GPa and ~470–490 °C. The temperature difference increased during the decompression up to ~50–100 °C during the LP/HT stage.
- The HP/LT event in the Ragua unit was recorded at ~2.2 GPa and ~480 °C. The LP/HT stage reached a temperature of ~535 °C.
- It is remarkable that similarities in the shapes of the P-T paths from the proposed units could imply the existence of a continuous sequence showing an inverted metamorphism, rather than a complex tectonically divided into several tectono-metamorphic units.
- Allanite dating of two samples one from the Bédar-Macael and one from the Calar-Alto units allowed us to interpret the date range of 13–15 Ma as the possible age of the LP/HT stage.

Supplementary data to this article can be found online at https://doi.org/10.1016/j.tecto.2019.06.028.

Acknowledgement

The authors like to express their gratitude to Hans-Joachim Massonne and Romain Augier for their stimulating comments and suggestions and Philippe Agard for his editorial handling. We acknowledge Daniela Rubatto and Jörg Hermann (Institute of Geological Sciences, University of Bern), and Jesús Galindo Zaldívar and Manuel Martínez Martos (Facultad de Ciencias, Universidad de Granada) for their comments and discussion on this work. This study was supported by the Ministerio de Economía y Competitividad (Spain) (Project CGL 2012-31872), and by the project DAMAGE (AEI/FEDER CGL 2016-80687-R).

References

Aerden, D., Sayab, M., 2008. From Adria- to Africa-driven orogenesis: evidence from porphyroblasts in the Betic Cordillera. Spain. J. Struct. l Geol. 30, 1272–1287.
Aerden, D., Bell, T.H., Puga, E., Sayab, M., Lozano, J.A., Díaz de Federico, A., 2013. Multi-stage mountain building vs. relative plate motions in the Betic Cordillera deduced from integrated microstructural and petrological analysis of porphyroblast inclusion trails. Tectonophysics 587, 188–206.
Agard, P., Augier, R., Monié, R., 2011. Shear band formation and strain localization on a regional scale: evidence from anisotropic rocks below a major detachment (Betic Cordilleras, Spain). J. Struct. Geol. 33, 114–131.
Airaghi, L., Janots, E., Lanari, P., de Sigoyer, J., Magin, V., 2019. Allanite petrochronology in fresh and retrogressed garnet-biotite metapelites from the Longmen Shan (eastern Tibet). J. Petrol. 60, 151–176.
Airaghi, L., Lanari, P., de Sigoyer, J., Guillot, S., 2017. Microstructural vs compositional preservation and pseudomorphic replacement of muscovite in deformed metapelites from the Longmen Shan (Sichuan, China). Lithos 282-283, 262–280.
Augier, R., Agard, P., Monié, P., Jolivet, L., Robin, C., Booth-Rea, G., 2005a. Exhumation, doming and slab retreat in the Betic Cordillera (SE Spain): in situ Ar-40/Ar-39 ages and P-T-d-t paths for the Nevado-Filabride complex. J. Metamorph. Geol. 23, 357–381.
Augier, R., Booth-Rea, G., Agard, P., Martínez-Martínez, J.M., Jolivet, L., Azañón, J.M., 2005b. Exhumation constraints for the lower Nevado-Filabride complex (Betic Cordillera, SE Spain): a Raman thermometry and Tweequ multiequilibrium thermobarometry approach. Bulletin de la Societé Géologique de France 176, 403–416.
Augier, R., Jolivet, L., Robin, C., 2005c. Late Orogenic doming in the eastern Betic Cordilleras: final exhumation of the Nevado-Filábride complex and its relation to basin genesis. Tectonics 24.
Azañón, J.M., Goffé, B., 1997. Ferro-Magnesiocarpholite-kyanite assembleges as record of the high-pressure, low-temperature metamorphism in central Alpujarride units, Betic cordillera (SE Spain). Eur. J. Mineral. 9, 1035–1051.
Bakker, H., de Jong, K., Helmers, H., Biermann, C., 1989. The geodynamic evolution of the Internal Zone of the Betic Cordilleras (south-east Spain): a model based on structural analysis and geothermobarometry, J. Metamorph. Geol. 7, 359–38.
Balanyá, J.C., García-Dueñas, V., 1987. Les directions structurales dans le domaine d'Alborán de part et d'autre du détroit de Gibraltar. C. R. Acad. Sci. II 304, 929–932.
Baxter, E.F., Caddick, M.J., Dragovic, B., 2017. Garnet: a rock-forming mineral petrochronometer. Rev. Mineral. Geochem. 83 (1), 469–533.
Behr, W.M., Platt, J.P., 2012. Kinematic and thermal evolution during two-stage exhumation of a Mediterranean subduction complex. Tectonics 31, TC4025.
Berger, A., Wehrens, P., Lanari, P., Zwingmann, H., Herweg, M., 2017. Microstructures, mineral chemistry and geochronology of white micas along a retrograde evolution: An example from the Aar massif (Central Alps, Switzerland). Tectonophysics 721, 179–195.
Berman, R.G., 1991. Thermobarometry using multi-equilibrium calculations: a new technique, with petrological applications. Can. Mineral. 29, 833–855.
Beyssac, O., Goffé, B., Chopin, C., Rouzaud, J.N., 2002. Raman spectra of carbonaceous material in metasediments: a new geothermometer. J. Metamorph. Geol. 20, 859–871.
Booth-Rea, G., Azañón, J.M., Goffé, B., Vidal, O., Martínez-Martínez, J.M., 2002. High-pressure, low-temperature metamorphism in the Alpujarride units outcropping in southeastern Betics (Spain). C. R. Geosci. 334 (Série II), 857–865.

Booth-Rea, G., Martínez-Martínez, J.M., Giaconia, F., 2015. Continental subduction, intracrustal shortening and coeval upper-crustal extension: P-T evolution of subducted south-Iberian paleomargin metapelites. Tectonophysics 663, 122–139.
Bouillin, J., Durand-Delga, M., Olivier, P., 1986. Betic-Rif and Tyrrhenian distinctive features, genesis and development stages. In: Wezel, F.C. (Ed.), The origin of arcs. Elsevier, Amasterdam, pp. 281–304.
Brouwer, H.A., 1926. Zur Tektonik der betischen Kordilleren. Geol. Rundsch. 17, 332–336.
Brown, M., 2007. Metamorphic conditions in orogenic belts: a record of secular change. Int. Geol. Rev. 49, 193–234.
Brown, M., 2014. The contribution of metamorphic petrology to understanding lithosphere evolution and geodynamics. Geosci. Front. 5, 553–569.
Burn, M., Lanari, P., Pettke, T., Engi, M., 2017. Non-matrix-matched standardisation in LA-ICP-MS analysis: general approach and application to allanite Th-U-Pb age-dating. J. Anal. Atom. Spectrom. 32, 1359–1377.
Caddick, M.J., Kohn, M.J., 2013. Garnet: witness to the evolution of destructive plate boundaries. Elements 9, 427–432.
Carminati, E., Wortel, M.J.R., Spakman, W., Sabadini, R., 1998. The role of slab detachment processes in the opening of the western-central Mediterranean basins: some geological and geophysical evidence. Earth Planet. Sci. Lett. 160, 651–665.
Cenki-Tok, B., Oliot, E., Rubatto, D., Berger, A., Engi, M., Janots, E., Thomsen, T.B., Manzotti, P., Regis, D., Spandler, C., Robyr, M., Goncalves, P., 2011. Preservation of Permian allanite within an Alpine eclogite facies shear zone at Mt Mucrone, Italy: mechanical and chemical behaviour of allanite during mylonitization. Lithos 125, 40–50.
Cenki-Tok, B., Darling, J., Rolland, Y., Dhuime, B., Storey, C.D., 2014. Direct dating of mid-crustal shear zones with synkinematic allanite: new in situ U-Th-Pb geochronological approaches applied to the Mont Blanc Massif. Terra Nova 26 (1), 29–37.
Chapman, A., Luffi, P., Saleeby, J., Petersen, S., 2011. Metamorphic evolution, partial melting and rapid exhumation above an ancient flat slab: insights from the San Emigdio Schist, southern California. J. Metamorph. Geol. 29 (6), 601–626.
Cheng, H., Cao, D., 2015. Protracted garnet growth in high-P eclogite: constraints from multiple geochronology and P–T pseudosection. J. Metamorph. Geol. 33, 613–632.
de Andrade, V., Vidal, O., Lewin, E., O'Brien, P., Agard, P., 2006. Quantification of electron microprobe compositional maps of rock thin sections: an optimized method and examples. J. Metamorph. Geol. 24, 655–668.
de Jong, K., 2003. Very fast exhumation of high-pressure metamorphic rocks with excess 40Ar and inherited 87Sr, Betic Cordilleras, southern Spain. Lithos 70, 91–110.
de Jong, K., Bakker, H.E., 1991. The Mulhacen and Alpujarride complexes in the Sierra de los Filabres. SE Spain: Litho-stratigraphy. Geol. Mijnbouw 70, 93–103.
Didon, J., Durand-Delga, M., Kornprobst, J., 1973. Homologies géologiques entre les deux rives du Détroit de Gibraltar. B. Soc. Geol. Fr. 15 (7), 77–105.
Durand-Delga, M., Fontboté, J.M., 1980. Le cadre structural de la Méditerranée occidentale. 26 Congrès. Géol. Intern., Paris. Les Chaînes alpines issues de la Téthys. Mém. B.R.G.M., 115, 67-85.
Egeler, C.G., Simon, O.J., 1969. Orogenic evolution of the Betic zone (Betic cordilleras, Spain), with emphasis on the nappe structures. Geol Mijnbouw 48, 296–305.
Engi, M., 2017. Petrochronology based on REE-minerals: monazite, allanite, xenotime, apatite. Rev. Mineral. Geochem. 83, 365–418.
Engi, M., Lanari, P., Kohn, M.J., 2017. Significant ages — an introduction to petrochronology. Rev. Mineral. Geochem. 83 (1), 1–12.
Ernst, W.G., 1988. Tectonic history of subduction zones inferred from retrograde blueschist P-T paths. Geology 16, 1081–1084.
Esteban, J.J., Sánchez-Rodríguez, L., Seward, D., Cuevas, J., Tubía, J.M., 2004. The late thermal history of the Ronda area, southern Spain. Tectonophysics 389 (1), 81–92.
Evans, T.P., 2004. A method for calculating effective bulk composition modification due to crystal fractionation in garnet-bearing schist: implications for isopleth thermobarometry. J. Metamorph. Geol. 22, 547–557.
Foster, G., Parrish, R.R., 2003. Metamorphic monazite and the generation of P-T-t paths. Geol. Soc. London Spec. Publ. 220, 25–47.
Gaidies, F., de Capitani, C., Abart, R., Schuster, R., 2008. Prograde garnet growth along complex P–T–t paths: results from numerical experiments on polyphase garnet from the Wölz Complex (Austroalpine basement). Contrib. Mineral. Petrol. 155, 673–688.
Galindo-Zaldívar, J., 1993. Geometría de las deformaciones neógenas en Sierra Nevada (Cordilleras Béticas). Tesis Universidad de Granada. Monografía Tierras del Sur, 249 p.
Galindo-Zaldívar, J., González-Lodeiro, F., Jabaloy, A., 1989. Progressive extensional shear structures in a detachment contact in the western Sierra Nevada (Betic Cordilleras, Spain). Geodin. Acta 3, 73–85.
García-Dueñas, V., Martínez-Martínez, J.M., Orozco, M., Soto, J., 1988. Plis-nappes, cisaillements syn- à post-métamorphiques et cisaillements ductiles-fragiles en distension dans les Nevado-Filabrides (Cordillères bétiques, Espagne). C. R. Geosci. 307, Série II, 1389-1395.
Gebauer, D., Schertl, H.-P., Brix, M., Schreyer, W., 1997. 35 Ma old ultrahigh-pressure meta- morphism and evidence for very rapid exhumation in the Dora Maira massif, Western Alps. Lithos 41, 5–24.
Giuntoli, F., Lanari, P., Engi, M., 2018. Deeply subducted continental fragments – part 1: fracturing, dissolution–precipitation, and diffusion processes recorded by garnet textures of the central Sesia Zone (western Italian Alps). Solid Earth 9 (1), 167–189.
Goffé, B., Michard, A., García-Dueñas, V., González-Lodeiro, F., Monié, P., Campos, J., Galindo-Zaldívar, J., Jabaloy, A., Martínez-Martínez, J.M., Simancas, F., 1989. First evidence of high-pressure, low temperature metamorphism in the Alpujárride nappes, Betic Cordillera (SE Spain). Eur. J. Mineral. y 1, 139–142.
Gómez-Pugnaire, M.T., Fernández-Soler, J.M., 1987. High-pressure metamorphism in metabasite from the Betic Cordilleras (SE Spain) and its evolution during the Alpine orogeny. Contrib. Mineral. Petrol. 95, 231–244.
Gómez-Pugnaire, M.T., Franz, G., Sánchez-Vizcaíno, V.L., 1994. Retrograde formation of NaCl-scapolite in high pressure metaevaporites from the Cordilleras Béticas (Spain). Contrib. Mineral. Petrol. 77, 619–640.
Gómez-Pugnaire, M.T., Rubatto, D., Fernández-Soler, J.M., Jabaloy, A., López-Sánchez-Vizcaíno, V., González-Lodeiro, F., Galindo-Zaldívar, J., Padrón-Navarta, J.A., 2012. U-Pb geochronology of Nevado-Filábride gneisses: evidence for the Variscan nature of the deepest Betic complex (SE Spain). Lithos 146-147, 93–111.
Guillot, S., Hattori, K., Agard, P., Schwartz, S., Vidal, O., 2009. Exhumation processes in oceanic and continental subduction contexts: a review. In: Lallemand, S., Funi-ciello, F. (Eds.), Subduction Zone Dynamics. Springer-Verlag, Berlin Heidelberg, pp. 175–204.
Hodges, K.V., Crowley, P.D., 1985. Error estimation and empirical geothermobarometry for pelitic systems. Am. Mineral. 70 (7-8), 702–709.
Holland, T.J.B., Powell, R., 1998. An internally consistent thermodynamic data set for phases of petrological interest. J. Metamorph. Geol. 16, 309–343.
Holland, T.J.B., Powell, R., 2011. An improved and extended internally consistent thermodynamic dataset for phases of petrological interest, involving a new equation of state for solids. J. Metamorph. Geol. 29, 333–383.
Jabaloy, A., Galindo-Zaldívar, J., González-Lodeiro, F., 1993. The Alpujarride-Nevado-Filábride extensional shear zone, Betic Cordilleras, SE Spain. J. Struct. Geol. 15, 555–569.
Jabaloy, A., Gómez-Pugnaire, M.T., Padrón-Navarta, J.A., López-Sánchez-Vizcaíno, V., Garrido, C.J., 2015. Subduction- and exhumation-related structures preserved in metaserpentinites and associated metasediments from the Nevado-Filábride Complex (Betic Cordillera, SE Spain). Tectonophysics 644-645, 40–57.
Jamienson, R.A., 1991. P-T-t paths of collisional orogens. Geol. Rundsch. 80 (2), 321–332.
Janots, E., Negro, F., Brunet, F., Goffé, B., Engi, M., Bouybaouène, M.L., 2006. Evolution of REE mineralogy in HP-LT metapelites of the Septide Complex, Rif, Morocco: monazite stability and geochronology. Lithos 87, 214–234.
Johnson, C., Harbury, N., Hurford, A.J., 1997. The role of extension in the Miocene denudation of the Nevado-FilábrideComplex, Betic Cordillera (SE Spain). Tectonics 16, 189–204.
Kirchner, K.L., Behr, W.M., Loewy, S., Stockli, D.F., 2016. Early Miocene subduction in the western Mediterranean: Constraints from Rb-Sr multimineral isochron geochronology. Geochem. Geophys. Geosyst. 17, 1842–1860.
Kohn, M.J., Spear, F.S., 1991. Error propagation for barometers; 2, application to rocks. Am. Mineral. 76 (1-2), 138–147.
Laborda-López, C., López Sánchez-Vizcaíno, V., Marchesi, C., Gómez-Pugnaire, M.T., Garrido, C.J., Jabaloy-Sánchez, A., Padrón-Navarta, J.A., Hidas, K., 2018. High pressure metamorphism of rodingites during serpentinite dehydration (cerro del almirez, southern spain): implications for the redox state in subduction zones. J. Metamorph. Geol. 36 (9), 1141–1173.
Lanari, P., Duesterhoeft, E., 2019. Modeling Metamorphic Rocks using Equilibrium Thermodynamics and Internally Consistent Databases: Past Achievements, Problems and Perspectives. J. Petrol. 60, 19–56.
Lanari, P., Engi, M., 2017. Local bulk composition effects on metamorphic mineral assemblages. Rev. Mineral. Geochem. 83, 55–102.
Lanari, P., Ferrero, S., Goncalves, P., Grosch, E., 2019. Metamorphic geology: progress and perspectives. Geol. Soc. London Spec. Publ. 478, 1–12.
Lanari, P., Giuntoli, F., Loury, C., Burn, M., Engi, M., 2017. An inverse modeling approach to obtain P-T conditions of metamorphic stages involving garnet growth and resorption. Eur. J. Mineral. 29, 181–199.
Lanari, P., Riel, N., Guillot, S., Vidal, O., Schwartz, S., Pêcher, A., Hattori, K., 2013. Deciphering high-pressure metamorphism in collisional context using microprobe-mapping methods: application to the Stak eclogitic massif (NW Himalaya). Geology 41, 111–114.
Lanari, P., Vho, A., Bovay, T., Airaghi, L., Centrella, S., 2019. Quantitative Compositional Mapping of Mineral Phases by Electron Probe Micro-analyser. Geol. Soc. Lond., Spec. Publ. 474, 39–63.
Lanari, P., Vidal, O., De Andrade, V., Dubacq, B., Lewin, E., Grosch, E.G., Schwartz, S., 2014. XMapTools: a MATLAB©-based program for electron microprobe X-ray image processing and geothermobarometry. Comput. Geosci. 62, 227–240.
Laurent, V., Lanari, P., Naïr, I., Augier, R., Lahfid, A., Jolivet, L., 2018. Exhumation of eclogite and blueschist (Cyclades, Greece): pressure-temperature evolution determined by thermobarometry and garnet equilibrium modelling. J. Metamorph. Geol. 36, 769–798.
Li, B., Massonne, H.J., 2018. Two tertiary metamorphic events recognized in high-pressure metapelites of the Nevado-Filábride Complex (Betic Cordillera, S Spain). J. Metamorph. Geol. 36, 603–630.
Lonergan, L., Johnson, C., 1998. Reconstructing orogenic exhumation histories using synorogenic detrital zircons and apatites: an example from the Betic Cordillera, SE Spain. Basin Res. 10 (3), 353–364.
López-Sánchez-Vizcaíno, V., Rubatto, D., Gómez-Pugnaire, M.T., Tommsdorff, V., Müntener, O., 2001. Middle Miocene high-pressure metamorphism and fast exhumation of the Nevado-Filábride Complex, SE Spain. Terra Nova 13, 327–332.
López-Sánchez-Vizcaíno, V., Trommsdorff, V., Gómez-Pugnaire, M.T., Garrido, C.J., Müntener, O., Connolly, J.A.D., 2005. Petrology of titanian clinohumite and olivine at the high-pressure breakdown of antigorite serpentinite to chlorite harzburgite (Almirez Massif, S. Spain). Contrib. Mineral. Petr. 149, 627–646.
Loury, C., Rolland, Y., Cenki-Tok, B., Lanari, P., Guillot, S., 2016. Late Paleozoic evolution of the South Tien Shan: insights from P–T estimates and allanite geochronology on retrogressed eclogites (Chatkal range, Kyrgyzstan). J. Geodyn. 96, 62–80.
Mäkel, G.H., 1985. The geology of the Malaguide Complex and its bearing on the geodynamic evolution of the Betic-Rif orogen (southern Spain and northern Morocco). GUA papers of Geology. Ser. 1, 22, 263 p.

Martínez-Martínez, J.M., 1986. Evolución tectono-metamórfica del Complejo Nevado-Filábride en el sector de unión entre Sierra Nevada y Sierra de los Filabres (Cordilleras Béticas). Cuadernos de Geología. Universidad de Granada 13, 1–194.
Martínez-Martínez, J.M., Soto, J.I., Balanyá, J.C., 2002. Orthogonal folding of extensional detachments: Structure and origin of the Sierra Nevada elongated dome (Betics, SE Spain). Tectonics 21, 1–22.
Massonne, H.-J., Schreyer, W., 1987. Phengite geobarometry based on the limiting assemblage with K-feldspar, phlogopite, and quartz. Contributions Mineral. Petrol. 96, 212–224.
Monié, P., Galindo-Zaldívar, J., González-Lodeiro, F., Goffé, B., Jabaloy, A., 1991. 40Ar/39Ar geochronology of Alpine tectonism in the Betic Cordilleras (southern Spain). J. Geol. Soc. London 148, 288–297.
Nelder, J.A., Mead, R., 1965. A simplex method for function minimization. Comput. J. 7, 308–313.
Padrón-Navarta, J.A., Hermann, J., Garrido, C.J., López-Sánchez-Vizcaíno, V., Gómez-Pugnaire, M.T., 2010. An experimental investigation of antigorite dehydration in natural silica-enriched serpentinite. Contrib. Mineral. Petrol. 159, 25–42.
Platt, J.P., Anczkiewicz, R., Soto, J.I., Kelley, S.P., Thirlwall, M., 2006. Early Miocene continental subduction and rapid exhumation in the western Mediterranean. Geology 34, 981–984.
Platt, J.P., Behr, W.M., Johansen, K., Williams, R., 2013. The Betic-Rif Arc and its Orogenic Hinterland: a review. Annu. Rev. Earth Planet. Sci. 41, 313–357.
Platt, J.P., Behrmann, J.H., 1986. Structures and fabrics in a crustal-scale shear zone, Betic Cordillera, SE Spain. J. Struct. Geol. 8, 15–33.
Platt, J.P., Kelley, S.P., Carter, A., Orozco, M., 2005. Timing of tectonic events in the Alpujárride Complex, Betic Cordillera. S. Spain. J. Geol. Soc. London 162, 451–462.
Puga, E., Díaz de Federico, A., 1976. Pre-Alpine metamorphism in the Sierra Nevada Complex (Betic Cordilleras Spain). Cuadernos de Geología 7, 161–171.
Puga, E., Díaz de Federico, A., Fontboté, J.M., 1974. Sobre la individualización y sistematización de las unidades profundas de la Zona Bética. Estudios Geológicos 30, 543–548.
Puga, E., Díaz de Federico, A., Nieto, J.M., 2002. Tectonostratigraphic subdivision and petrological characterisation of the deepest complexes of the Betic zone: a review. Geodin. Acta 15, 23–43.
Puga, E., Nieto, J.M., De Federico, A.D., 2000. Contrasting P-T paths in eclogites of the Betic Ophiolitic Association, Mulhacen Complex, southeastern Spain. Can. Mineral. 38, 1137–1161.
Putnis, A., 2009. Mineral replacement reactions. Rev. Mineral. Geochem. 70, 87–124.
Regis, D., Rubatto, D., Darling, J., Cenki-Tok, B., Zucali, M., Engi, M., 2014. Multiple metamorphic stages within an eclogite-facies terrane (Sesia Zone, Western Alps) revealed by Th–U–Pb petrochronology. J. Petrol. 55 (7), 1429–1456.
Rolland, Y., Lardeaux, J.-M., Jolivet, L., 2012. Deciphering orogenic evolution. J. Geodyn. 5, 6–57.
Rubatto, D., Hermann, J., 2001. Exhumation as fast as subduction? Geology 29, 3–6.
Rubatto, D., Regis, D., Hermann, J., Boston, K., Engi, M., Beltrando, M., McAlpine, S., 2011. Yo-Yo subduction recorded by accessory minerals in Italian Western Alps. Nat. Geosci. 4, 338–342.
Rubatto, D., Scambelluri, M., 2003. U–Pb dating of magmatic zirconand metamorphic baddeleyte in the Ligurian eclogites (Voltri Massif, Western Alps). Contrib. Mineral. Petrol. 146, 341–355.
Ruiz-Cruz, M.D., Sanz de Galdeano, C., Santamaría, A., 2015. Petrology and thermobarometric estimates for metasediments, orthogneisses, and eclogites from the Nevado-Filábride Complex in the Western Sierra Nevada (betic Cordillera, Spain). Can. Mineral. 53 (6), 1083–1107.
Sánchez-Rodríguez, L., Gebauer, D., 2000. Mesozoic formation of pyroxenites and gabbros in the Ronda area (southern Spain), followed by Early Miocene subduction metamorphism and emplacement into the middle crust: U–Pb sensitive high-resolution ion microprobe dating of zircon. Tectonophysics 316, 19–44.
Santamaría-López, A., Sanz de Galdeano, C., 2018. SHRIMP U–Pb detrital zircon dating to check subdivisions in metamorphic complexes: a case of study in the Nevado–Filábride complex (Betic Cordillera, Spain). Int. J. Earth Sci. 107 (7), 2539–2552.
Sanz de Galdeano, C., El Kadiri, K., Simancas, F., Rachid, H., López-Garrido, A.C., El Mrihi, A., Chalouan, A., 2006. Paleogeographical reconstruction of the Malaguide-Ghomaride Complex (Internal Betic-Rifian Zone) based on Carboniferous granitoid pebble provenance. Geol. Carpath. 57, 327–336.
Sanz de Galdeano, C., López-Garrido, A.C., 2016. The Nevado-Filábride Complex in the western part of Sierra de los Filabres (Betic Internal Zone). Structure and lithological succession. Boletín Geológico y Minero 127 (4), 823–836.
Sanz de Galdeano, C., López-Garrido, A.C., Santamaría-López, A., 2016. Major scale structure of the marbles situated between Cóbdar and Macael (Nevado-Filabride Complex, Betic Cordillera, Almería province, Spain), and general stratigraphic arrangement. Revista de la Sociedad Geológica de España 29 (2), 107–116.
Sláma, J., Košler, J., Condon, D.J., Crowley, J.L., Gerdes, A., Hanchar, J.M., Horstwood, M.S., Morris, G.A., Nasdala, L., Norberg, N., 2008. Plešovice zircon – a new natural reference material for U–Pb and Hf isotopic microanalysis. Chem. Geol. 249, 1–35.
Spear, F.S., 1988. Metamorphic fractional crystallization and internal metasomatism by diffusional homogenization of zoned garnets. Contrib. Mineral. Petrol. 99 (4), 507–517.
Thompson, A.B., England, P.C., 1984. Pressure temperature time paths of regional metamorphism. 2. Their inference and interpretation using mineral assemblages in metamorphic rocks. Journal of Petrology 25, 929–955.
Tinkham, D.K., Ghent, E.D., 2005. Estimating P-T conditions of garnet growth with isochemical phase-diagrams sections and the problem of effective bulk-composition. Can. Mineral. 43 (1), 35–50.
Vera, J.A., 2004. Las Zonas Internas Béticas in: Vera, J.A. (Ed.), Geología de España, Madrid, 385-437.
Vissers, R., 1981. A structural study of the central Sierra de los Filabres (Betic zone, SE Spain) with emphasis on deformational processes and their relation to the Alpine metamorphism, PhD thesis, 154 pp., Univ. of Amsterdam, Amsterdam.
Vissers, R., Platt, J.P., van der Wal, D., 1995. Late orogenic extension of the Betic Cordillera and the Alborán Domain: a lithospheric view. Tectonics 14, 786–803.
Worley, B., Powell, R., 2000. High-precision relative thermobarometry: theory and a worked example. J. Metamorph. Geol. 18 (1), 91–101.
Yakymchuk, C., Clark, C., White, R., 2017. Phase relations, reaction sequences and petrochronology: methods and applications. Rev. Mineral. Geochem. 83, 13–53.
Zeck, H.P., 2004. Rapid exhumation in the Alpine Belt of the Betic-Rif (W Mediterranean): tectonic extrusion. Pure Appl. Geophys. 161, 477.